

# Enhanced Photocatalytic Performance in Chromium(VI) Reduction and Dye Degradation using Sn<sub>3</sub>O<sub>4</sub>/SnS<sub>2</sub> Nanocomposite and Mechanism Insight

Gandharve Kumar

Indian Institute of Technology Roorkee

Rajkumar Dutta (✉ [r.dutta@cy.iitr.ac.in](mailto:r.dutta@cy.iitr.ac.in))

Indian Institute of Technology Roorkee <https://orcid.org/0000-0001-9667-0399>

---

## Research Article

**Keywords:** Sn<sub>3</sub>O<sub>4</sub>/SnS<sub>2</sub> nanocomposite, solar photocatalyst, Z-scheme heterojunction, photocatalytic reduction of Cr (VI) and photocatalytic degradation of methylene blue, degradation product analysis by UPLC-Q-Tof-MS

**Posted Date:** December 23rd, 2021

**DOI:** <https://doi.org/10.21203/rs.3.rs-1107930/v1>

**License:** © ⓘ This work is licensed under a Creative Commons Attribution 4.0 International License.

[Read Full License](#)

---

1 **Enhanced photocatalytic performance in chromium (VI) reduction and dye**  
2 **degradation using Sn<sub>3</sub>O<sub>4</sub>/SnS<sub>2</sub> nanocomposite and mechanism insight**

3 Gandharve Kumar<sup>1</sup>, Raj Kumar Dutta<sup>1,2,\*</sup>

4 <sup>1</sup>Centre of Nanotechnology, Indian Institute of Technology Roorkee, Roorkee-247667, India

5 <sup>2</sup>Department of Chemistry, Indian Institute of Technology Roorkee, Roorkee-247667, India

6 \* Author for Correspondence: Email: [r.dutta@cy.iitr.ac.in](mailto:r.dutta@cy.iitr.ac.in) (R.K. Dutta)

7 **Abstract**

8 Detection of residual organic and inorganic species in water bodies including drinking water  
9 has led to developing strategies for their removal. Here we report a very efficient method of  
10 photoreduction of Cr (VI) and photodegradation of methylene blue dye in aqueous medium  
11 using Z-scheme heterojunction based Sn<sub>3</sub>O<sub>4</sub>/SnS<sub>2</sub> solar photocatalyst. The photocatalyst is  
12 synthesized by hydrothermal route and it is thoroughly characterized in terms of its structural,  
13 compositional, morphological and optical properties. About 100 % of Cr (VI) reduction in 60  
14 min and 99.6 % of methylene blue degradation in 90 min is achieved under sunlight exposure  
15 at a photocatalytic rate of 0.066 min<sup>-1</sup> and 0.043 min<sup>-1</sup>, respectively. The total organic carbon  
16 estimation of the post-degradation reaction medium corresponded to 85.1 % (MB)  
17 mineralization. The photocatalytic degradation is attributed to *in-situ* generation of reactive  
18 oxygen species (ROS) e.g., superoxide radicals, hydroxide radicals, and the role of ROS  
19 towards reduction and degradation of Cr (VI) and MB respectively, is confirmed from ROS  
20 scavenging studies. The dye degradation mechanism has been discussed by analyzing the  
21 degradation products via UPLC-Q-Tof-MS. The photocatalytic degradation of methylene  
22 blue by Sn<sub>3</sub>O<sub>4</sub>/SnS<sub>2</sub> nanocomposites is significantly enhanced as compared to SnS<sub>2</sub>  
23 photocatalyst, attributed to Z-scheme heterojunction and the charge carrier mobility.

## 24 **Keywords**

25 Sn<sub>3</sub>O<sub>4</sub>/SnS<sub>2</sub> nanocomposite, solar photocatalyst; Z-scheme heterojunction; photocatalytic  
26 reduction of Cr (VI) and photocatalytic degradation of methylene blue; degradation product  
27 analysis by UPLC-Q-Tof-MS.

## 28 **Introduction**

29 Water bodies contaminated with inorganic and organic species has a cascading impact  
30 on ecosystem and also a major cause of human health hazard (Barrera-Díaz et al. 2012;  
31 Coetzee et al. 2020; Tumolo et al. 2020). Among these, Cr (VI) and organic dyes in industrial  
32 as well as municipal wastewater are some of the most common constituents owing to their  
33 wide range of usages. For example, Cr (VI) compounds are used in electroplating, leather  
34 tanning, metal finishing, textile production, and dyeing (He et al. 2020; Karimi-Maleh et al.  
35 2021). Consequently, large volumes of aqueous chromium wastes are generated and  
36 discharged into the environment without pretreatment (Owlad et al. 2009). Chromium  
37 compounds mostly exist in two standard oxidation states, i.e., Cr (III) and Cr (VI). Out of  
38 which, Cr (VI) is water soluble and it is highly toxic owing to its carcinogenic nature  
39 (Sedman et al. 2006; Narayani and Shetty 2013). On the other hand, Cr (III) is less toxic and  
40 can readily be precipitated out of a solution as Cr(OH)<sub>3</sub> (Mertz 1993). Similarly, organic dyes  
41 are widely used in textile industries for the colouring of fabrics such silk, cotton and wool etc  
42 (Khatri et al. 2015). These dyes are generally stable, highly water soluble, non-biodegradable  
43 and carcinogenic in nature, and hence they are hazardous to human and aquatic species  
44 (Gusain et al. 2019; Yaseen and Scholz 2019). This demands scientific attention for  
45 developing efficient technologies for removal or elimination of Cr (VI) and organic dyes  
46 from wastewater. The conventional remediation processes such coagulation, adsorption,  
47 membrane separation and precipitation are insufficient for complete removal of the

48 hexavalent chromium and organic dyes from water and wastewater (Hafiane et al. 2000;  
49 Katheresan et al. 2018). The efficiency of biodegradation of Cr (VI) and organic dyes is low.  
50 In view of this, advanced oxidation process (AOP) is considered to be more efficient,  
51 particularly for treating organic pollutants as it tends to mineralize the pollutants (Bethi et al.  
52 2016). However, AOP is associated to higher operational cost and due to generation of  
53 secondary wastes. Alternately, heterogeneous semiconductor-based photocatalysis have  
54 gained major attention from the researchers for the treatment of polluted wastewater as it also  
55 has the capacity to mineralize the organic constituents (Saadati et al. 2016; Calvete et al.  
56 2019; Di et al. 2019; Wei et al. 2020). Here light of energy greater than the band gap of the  
57 photocatalyst is needed for generating electrons and holes which are retained in  
58 thermodynamically favorable band edges, i.e., conduction band of one semiconductor  
59 materials and valence band of the other semiconducting material (Zhang et al. 2020; Wang et  
60 al. 2021). The charge carriers can diffuse to the outer surface of the photocatalyst to interact  
61 with H<sub>2</sub>O and molecular oxygen at the outer surface of the photocatalyst to produce highly  
62 reactive oxygen species (ROS). This ROS in turn can cleave the bonds of the pollutants (e.g.,  
63 dye molecules) and eventually mineralize. The major hurdles this system is associated with  
64 favourable recombination of charge carriers, loss of charge carriers due to their trapping in  
65 defect sites, poor redox property owing to band energy mismatch for ROS generation (Das  
66 and Dutta 2015; Sharma and Dutta 2018; Wang et al. 2020). In addition, most photocatalytic  
67 degradation studies are based on UV light exposure, which is a major limitation from solar  
68 harvesting technology point of view as only 6 % of the sunlight constitutes UV range  
69 (Mukherjee et al. 2021). Considering all the above conditions, it may be put forward that Z-  
70 type heterojunction based photocatalyst is favourable for enhancing photocatalytic  
71 performance as demonstrated in literature (Qiang et al. 2021). The main advantage with these  
72 Z-type heterojunction is attributed to efficient inhibition of charge carrier recombination and

73 also decrease the defect state density (Lin et al. 2021). It is mostly found that the  
74 photocatalysts with Z-type heterojunction are made of oxides like (Li et al. 2016; Huang et al.  
75 2019; Zhao et al. 2019; Xu et al. 2020). Contrastingly, studies based on Z-type photocatalyst  
76 made of oxides-sulphide mixed systems are much less (Di et al. 2019). One of the main  
77 concern here is the stability of the sulphide component. Considering these conditions, we  
78 present here a novel Z-type heterojunction photocatalyst comprising a low band gap  $\text{SnS}_2$  as a  
79 base material in combination with  $\text{Sn}_3\text{O}_4$  which is a large band gap materials. The  
80 photocatalyst, represented as  $\text{Sn}_3\text{O}_4/\text{SnS}_2$  nanocomposites, has been thoroughly characterized  
81 and was studied sunlight mediated photoreduction of hexavalent chromium Cr (VI) and  
82 photocatalytic degradation of organic dye in aqueous medium. Hexavalent Chromium Cr (VI)  
83 and methylene blue has been chosen as a model pollutants, as it has been detected in  
84 ecosystem comprising river water, ground water, sediments and soils, and in drinking water  
85 (Fick et al. 2009; Sharma and Bhattacharya 2017; Singh et al. 2019; Khan et al. 2020). The  
86 detailed methodology for synthesis, characterization and photocatalytic degradation kinetics  
87 by  $\text{Sn}_3\text{O}_4/\text{SnS}_2$  nanocomposites has been discussed. The mechanism of photocatalytic  
88 degradation of methylene blue has been discussed in the light of in-situ generated reactive  
89 oxygen species (ROS) and identification of degradation products by UPLC-Q-Tof-MS  
90 technique.

## 91 **Experimental section**

### 92 **Chemicals**

93 Stannous chloride dihydrate (98%),stannous chloride pentahydrate  
94 (98%),thioacetamide, sodium hydroxide, trisodium citrate, diphenylcarbazine, chloroform,  
95 tert-butanol, ammonium oxalate, potassium dichromate, and ethanol (99%) were procured  
96 from HiMedia Pvt. Ltd., India. All precursors used in this study were of analytical grade and

97 were used without further purification. Analytical grade deionized water (Millipore) was used  
98 throughout the study.

### 99 **Synthesis Sn<sub>3</sub>O<sub>4</sub>/SnS<sub>2</sub> NCs**

100 It is a two-step process, where Sn<sub>3</sub>O<sub>4</sub> nanoflakes were first prepared via hydrothermal  
101 route. In a typical process, 4 mmol of Stannous chloride dihydrate was dissolved in 12.5 mL  
102 deionized water than 12.5 mmol tri-sodium citrate dihydrate was added and stirred until a  
103 transparent solution was obtained, then 0.1 g of sodium hydroxide dissolved in 12.5 mL D.I  
104 water, was added to the above solution dropwise and stir for 1 h and finally transfer the  
105 solution into a 50 mL Teflon jar and heated at 180 °C for 12 h in a microprocessor-based  
106 temperature-controlled furnace. Finally, the autoclave was cooled to room temperature. The  
107 resulting solution of Sn<sub>3</sub>O<sub>4</sub> was then precipitated with ethanol and recovered by centrifuging  
108 at 15,000 rpm for 5 min. The batch of Sn<sub>3</sub>O<sub>4</sub> was washed several times with ethanol and then  
109 dried overnight in oven at 40°C.

110 Next 5.0 mmol SnCl<sub>4</sub>.5H<sub>2</sub>O was dissolved in 40 mL deionized water than 12.5 mmol  
111 of Thioacetamide was added and stir until a homogenous solution was formed. After that, a  
112 definite wt.% of Sn<sub>3</sub>O<sub>4</sub> (i.e., 5 wt.%, 7 wt.% and 10 wt.%) was added to the above solution  
113 mixture under constant stirring. The whole mixture was then transferred to an autoclave and  
114 heated at 180°C for 8 h. The obtained precipitate was washed with deionised water and  
115 ethanol by centrifuging at 7000 rpm for 10 min and the final yellow product was dried at  
116 60°C overnight. The nanocomposites will be denoted as 0.05Sn<sub>3</sub>O<sub>4</sub>/SnS<sub>2</sub>, 0.07Sn<sub>3</sub>O<sub>4</sub>/SnS<sub>2</sub>  
117 and 0.10Sn<sub>3</sub>O<sub>4</sub>/SnS<sub>2</sub> according to the wt.% of precursor Sn<sub>3</sub>O<sub>4</sub> added. Likewise, control batch  
118 of pristine SnS<sub>2</sub> was prepared following the same synthetic protocol without the addition of  
119 Sn<sub>3</sub>O<sub>4</sub> nanoparticles.

120

## 121 **Characterization's techniques**

122 The as-synthesized batches of Sn<sub>3</sub>O<sub>4</sub>/SnS<sub>2</sub> NCs with different Sn<sub>3</sub>O<sub>4</sub> weight ratios,  
123 together with those of SnS<sub>2</sub> nanoparticles, Sn<sub>3</sub>O<sub>4</sub> nanoparticles are characterized by powder  
124 X-ray Diffraction, X-ray photoelectron spectroscopy, field emission scanning electron  
125 microscopy, high resolution transmission electron microscopy, Brunauer-Emmett-Teller  
126 (BET) specific surface area technique, photoluminescence spectroscopy, electrochemical  
127 impedance spectroscopy and by diffused reflectance spectroscopy. The details of these  
128 techniques and sample preparation are given as Supporting Information (Section S1).

129 The degradation intermediates were identified by UPLC (ACQUITY I) coupled to  
130 QToF (XeVO G2-XS QToF). Mobile phase A was aqueous formic acid solution (0.1%, v/v),  
131 and mobile phase B was acetonitrile. The gradient solvent was at a flow rate of 0.3 mL/min.  
132 The MS was performed in a positive ion mode using an electrospray ionization (ESI+) source  
133 under the following conditions: capillary voltage: 2.0 kV; gas (N<sub>2</sub>) flow rate: 50 L/h; gas  
134 temperature: 300 °C; nebulization pressure: 15 psi; scan time: 0.5 second.

## 135 **Evaluation of Photocatalytic activity**

136 The photocatalytic activities of the Sn<sub>3</sub>O<sub>4</sub>/SnS<sub>2</sub> NCs and their respective individual  
137 components (e.g., Sn<sub>3</sub>O<sub>4</sub> NPs, SnS<sub>2</sub> NPs) as photocatalysts were evaluated by monitoring the  
138 photocatalytic reduction of Cr (VI) solution (50 mg L<sup>-1</sup>) under natural sunlight irradiation. In  
139 a typical experiment, first, the pH of the initial 100 mL Cr (VI) solution was adjusted to 2.5  
140 by adding 1M H<sub>2</sub>SO<sub>4</sub> solution, then 50 mg of respective photocatalyst were dispersed in the  
141 batches of Cr (VI) solution (50 mg/L based on Cr in K<sub>2</sub>Cr<sub>2</sub>O<sub>7</sub> solution) taken in 250 mL  
142 beakers. This will be referred to as reaction assembly, which was subjected to slow  
143 continuous stirring (less than 100 rpm) for 60 min in dark condition to establish adsorption-  
144 desorption equilibrium. After 60 min the reaction assemblies was kept under natural sunlight

145 (photocatalytic experiments were carried out at IIT Roorkee (29°51'N; 77°53'E) in the month  
146 of April and May 2021. The solar irradiance was assumed to be 221 W/m<sup>2</sup> during the  
147 experiment day (Ramachandra et al. 2011). At regular intervals, 1.5 mL of the suspension  
148 was withdrawn from each reaction assembly and centrifuged at 15000 rpm for 2 min to  
149 discard any particles using Beckman Coulter Allegra TM X-22R. The concentration of Cr  
150 (VI) was monitored according to the previously reported method (Zhang et al. 2019). First,  
151 1.0 ml of the sample was mixed with 9 ml of 0.2 M H<sub>2</sub>SO<sub>4</sub> in a 10.0 ml volumetric flask.  
152 Subsequently, 0.2 ml of freshly prepared 1,5-diphenylcarbazine (250 mg/50 mL) solution was  
153 added to the above mixture. After shaking up the mixture, the solution was allowed to stand  
154 for 10-15 min to ensure full-color development. Subsequently, the solution was measured at  
155 540 nm by UV-vis spectrophotometer (Shimadzu, UV-2400, Japan). The effect of solution  
156 pH on the photoreduction efficiency of Cr (VI) was investigated under the same condition.  
157 The chromium solution with different pH was adjusted by 0.2 M H<sub>2</sub>SO<sub>4</sub> or NaOH.  
158 Organic dye methylene blue (MB) was selected as another target pollutant. The degradation  
159 of dye solution by the Sn<sub>3</sub>O<sub>4</sub>/SnS<sub>2</sub> NCs were carried out under the similar conditions as  
160 discussed above. Typically, 100 mL of MB dye solution (20 mg/L) treated with 50mg of  
161 pristine SnS<sub>2</sub>, Sn<sub>3</sub>O<sub>4</sub> and the batches of Sn<sub>3</sub>O<sub>4</sub>/SnS<sub>2</sub> as photocatalyst respectively and kept  
162 under slow continuous stirring (less than 100 rpm) for 60 min in dark conditions to establish  
163 adsorption- desorption equilibrium. The concentration variation of MB dye solution was  
164 examined by recording the absorbance of the supernatant liquid at its  $\lambda_{\max}$  of 664 nm, using  
165 UV-Vis spectrophotometer (UV-1800, Shimadzu, Japan).

166 The leached concentrations of respective constituents in the photocatalysts, viz. Sn  
167 from the batch of Cr (VI) solution treated with 0.07Sn<sub>3</sub>O<sub>4</sub>/SnS<sub>2</sub> NCs were determined by  
168 ICP-OES. The details of sample preparation are given as supporting information (Section  
169 S2). The photostability and re-usability of the best performing photocatalyst, i.e.,

170 0.07Sn<sub>3</sub>O<sub>4</sub>/SnS<sub>2</sub> NCs was assessed by monitoring photocatalytic reduction of Cr (VI) for five  
171 successive cycles. At the end of each cycle, the used photocatalyst was recovered, dried, and  
172 reused for the next cycle. After completing five cycles of photocatalytic reduction, the  
173 stability of the photocatalyst was studied by XRD and FESEM.

## 174 **Results and Discussion**

175 The powder X-ray diffraction (XRD) method was used to investigate the crystalline  
176 structure and phase composition of the as-synthesized batches of Sn<sub>3</sub>O<sub>4</sub>, SnS<sub>2</sub> and the  
177 Sn<sub>3</sub>O<sub>4</sub>/SnS<sub>2</sub> NCs. The characteristic Bragg reflection peaks for pristine SnS<sub>2</sub> were detected at  
178  $2\theta=14.8^\circ, 28.1^\circ, 32.0^\circ, 33.5^\circ, 46.0^\circ, 49.9^\circ$  and  $52.4^\circ$  (Fig. 1), which can be indexed to the (0  
179 0 1), (1 0 0), (0 0 2), (1 0 1), (0 0 3), (1 1 0) and (1 1 1) crystal planes of SnS<sub>2</sub> hexagonal  
180 phase. (JCPDS Card no.89-2358). Similarly, the characteristic Bragg diffraction peaks for  
181 pristine Sn<sub>3</sub>O<sub>4</sub> NPs were detected at  $2\theta = 26.9^\circ, 32.1^\circ, 37.0^\circ, \text{ and } 51.7^\circ$  (Fig.1), which were  
182 indexed to the (1 1 1), (1 2 2), (1 3 0), and (1 3 2) planes of triclinic Sn<sub>3</sub>O<sub>4</sub>, respectively  
183 (JCPDS Card No.- 16- 0737). The XRD pattern of 0.05Sn<sub>3</sub>O<sub>4</sub>/SnS<sub>2</sub> displayed characteristic  
184 peaks of pristine SnS<sub>2</sub> along with few smaller intensity peaks corresponding to Sn<sub>3</sub>O<sub>4</sub> (Table-  
185 S1). The intensity of the diffraction peaks of Sn<sub>3</sub>O<sub>4</sub> increased for the batches of  
186 0.07Sn<sub>3</sub>O<sub>4</sub>/SnS<sub>2</sub> and 0.10Sn<sub>3</sub>O<sub>4</sub>/SnS<sub>2</sub>, indicating gradual coverage of Sn<sub>3</sub>O<sub>4</sub> nanoparticles on  
187 SnS<sub>2</sub> surface. The detail information about crystallite sizes of the batches of Sn<sub>3</sub>O<sub>4</sub>/SnS<sub>2</sub> NCs  
188 and SnS<sub>2</sub> were discuss in the supporting information (Section S3).

189 The morphology of Sn<sub>3</sub>O<sub>4</sub>/SnS<sub>2</sub> NCs, along with their respective components e.g.,  
190 SnS<sub>2</sub> nanoparticles and Sn<sub>3</sub>O<sub>4</sub> nanoflakes were analysed by electron microscopy (given as  
191 Supporting Information, Fig. S1). The FE-SEM image of pure SnS<sub>2</sub> completely composed of  
192 clusters of nanoparticles with diameters in the range of 80–100 nm (Fig S1a). Sn<sub>3</sub>O<sub>4</sub> was  
193 composed of relatively smooth irregular nanoflakes of size ranging in between 100-400 nm  
194 long and thickness about 10 nm (Fig S1b). The FE-SEM image of 0.07Sn<sub>3</sub>O<sub>4</sub>/SnS<sub>2</sub> NCs

215 mostly revealed nanoclusters of SnS<sub>2</sub>, which is the major component in the nanocomposites,  
216 along with distribution of irregular shaped nanoflakes of Sn<sub>3</sub>O<sub>4</sub> (Fig S1c-d). The energy  
217 dispersive X-ray (EDX) spectrum of 0.07Sn<sub>3</sub>O<sub>4</sub>/SnS<sub>2</sub> NCs revealed the characteristic X-rays  
218 of Sn, S, and O. (Fig S1e), which indicated about formation of heterostructures of  
219 Sn<sub>3</sub>O<sub>4</sub>/SnS<sub>2</sub>. The morphology of the batch of 0.07Sn<sub>3</sub>O<sub>4</sub>/SnS<sub>2</sub> NCs was better revealed from  
220 the transmission electron microscopy (TEM) images. Here both nanoclusters of SnS<sub>2</sub> and  
221 irregular shaped Sn<sub>3</sub>O<sub>4</sub> nanoflakes could be observed corresponding to formation of  
222 Sn<sub>3</sub>O<sub>4</sub>/SnS<sub>2</sub> nanocomposites (Fig. 2a). The SnS<sub>2</sub> nanoclusters were 80-100 nm long and the  
223 sizes of Sn<sub>3</sub>O<sub>4</sub> were in the range of 50-70 nm long and about 10 to 15 nm in width. The  
224 formation of heterostructures of Sn<sub>3</sub>O<sub>4</sub>/SnS<sub>2</sub> is evident from the higher resolution TEM image  
225 which revealed heterojunction of SnS<sub>2</sub> nanoclusters and the irregular shaped Sn<sub>3</sub>O<sub>4</sub>  
226 nanoflakes (Fig. 2b). The crystalline nature of Sn<sub>3</sub>O<sub>4</sub>/SnS<sub>2</sub> NCs is revealed from the lattice  
227 fringes with corresponded to binary materials with interatomic layer spacing of 0.314 nm and  
228 0.330 nm (Fig. 2c). They correspond to the (1 0 0) lattice plane of hexagonal SnS<sub>2</sub> and (1 1 1)  
229 plane of triclinic Sn<sub>3</sub>O<sub>4</sub>, respectively. The selected area electron diffraction (SAED) pattern  
230 confirmed the strong interference patterns due to polycrystalline nature of Sn<sub>3</sub>O<sub>4</sub>/SnS<sub>2</sub> NCs  
231 (Fig. 2d). The results of XRD, FESEM and TEM confirmed formation of Sn<sub>3</sub>O<sub>4</sub>/SnS<sub>2</sub>  
232 heterostructure.

233 The proposed structure of 0.07Sn<sub>3</sub>O<sub>4</sub>/SnS<sub>2</sub> was further corroborated by compositional  
234 analysis of tin (Sn), oxygen (O) and sulphur elements by XPS measurement (Fig. 3a). The  
235 binding energy peaks of Sn 3d shows two peaks at 486.88 eV and 495.29 eV, which are  
236 assigned to Sn 3d<sub>5/2</sub> and Sn 3d<sub>3/2</sub>, respectively, suggesting the presence of Sn<sup>4+</sup> in  
237 0.07Sn<sub>3</sub>O<sub>4</sub>/SnS<sub>2</sub> (Fig. 3b). The binding energy peaks of S 2p displays a two strong peak at  
238 161.72 eV and 162.85 eV corresponding to S 2p<sub>3/2</sub> and S 2p<sub>1/2</sub>, respectively, which was  
239 attributed to the S<sup>2-</sup> state (Fig. 3c). The O1s binding energy peak is deconvoluted into two

220 peaks at 532.03 eV and 531.13 eV (Fig. 3d). The peaks corresponded to O-Sn<sup>4+</sup> bond and O-  
221 Sn<sup>2+</sup>, respectively, which are relevant to the proposed structural constituent of  
222 0.07Sn<sub>3</sub>O<sub>4</sub>/SnS<sub>2</sub> NCs. Therefore, the XPS results are consistent with the XRD and HRTEM  
223 findings shown above. This further provides more evidence that the obtained 0.07Sn<sub>3</sub>O<sub>4</sub>/SnS<sub>2</sub>  
224 composite consists of SnS<sub>2</sub> and Sn<sub>3</sub>O<sub>4</sub>.

225 The specific surface area of pristine SnS<sub>2</sub> and 0.07Sn<sub>3</sub>O<sub>4</sub>/SnS<sub>2</sub> NCs were analysed by  
226 N<sub>2</sub> adsorption-desorption isotherms and information about its porous nature was obtained  
227 from the BJH pore size distribution plot (Table S2). The BET plot of pure SnS<sub>2</sub> and  
228 0.07Sn<sub>3</sub>O<sub>4</sub>/SnS<sub>2</sub> NCs revealed type-IV isotherm (Fig. 4) and the corresponding BET surface  
229 area was determined as 55.06 m<sup>2</sup> g<sup>-1</sup> and 60.44 m<sup>2</sup> g<sup>-1</sup>, respectively. The growth of Sn<sub>3</sub>O<sub>4</sub>  
230 nanoflakes on the surface of the SnS<sub>2</sub> surface increased the surface areas and the pore volume  
231 of the 0.07Sn<sub>3</sub>O<sub>4</sub>/SnS<sub>2</sub> composites (Table S2). A narrow pore size distribution between 2-4  
232 nm is obtained (inset of Fig. 4), which suggested mesoporous nature of the 0.07Sn<sub>3</sub>O<sub>4</sub>/SnS<sub>2</sub>  
233 NCs. The mesoporous nature is also corroborated from the Type-IV isotherm plot (Peng et al.  
234 2015). The high surface area and mesoporous structures of the 0.07Sn<sub>3</sub>O<sub>4</sub>/SnS<sub>2</sub> composites,  
235 which is favourable for better interaction with pollutant molecules for adsorption and  
236 photocatalytic degradation.

237 The band gap of the as-synthesized batches of Sn<sub>3</sub>O<sub>4</sub>/SnS<sub>2</sub> NCs and its constituents,  
238 e.g., pristine batches of SnS<sub>2</sub> NPs and Sn<sub>3</sub>O<sub>4</sub> NPs were determined from diffused reflectance  
239 spectroscopy studies. The pristine Sn<sub>3</sub>O<sub>4</sub> nanoflakes and Sn<sub>3</sub>O<sub>4</sub>/SnS<sub>2</sub> NCs strongly  
240 absorbance in the UV and visible light region (Fig. S2), whereas the SnS<sub>2</sub> nanoclusters absorb  
241 only in the visible region (Fig. S2). The diffused reflectance spectra were converted to  
242 absorption spectra using conventional Kubelka-Munk function (Kortüm 1969), and the  
243 optical band gap was determined from Tauc plot given as, (Tauc et al. 1966)

244  $(\alpha h\nu)^{1/n} = A(h\nu - E_g).$

245 In this equation  $\alpha$ ,  $h$ ,  $\nu$  and  $A$  refers to the absorption coefficient, Planck's constant, incident  
246 light frequency and proportionality constant, respectively. The value of 'n' is considered  
247 according to the nature of electronic transition, i.e.  $n = \frac{1}{2}$  for direct transition and  $n = 2$  for  
248 indirect transition. The Tauc's plots of  $0.05\text{Sn}_3\text{O}_4/\text{SnS}_2$  NCs,  $0.07\text{Sn}_3\text{O}_4/\text{SnS}_2$  NCs,  
249  $0.10\text{Sn}_3\text{O}_4/\text{SnS}_2$  NCs and  $\text{SnS}_2$  nanoclusters are given in Fig. 5. The band gap of these  
250 materials were estimated by extrapolating the linear part of the respective Tauc plots to  $(\alpha h\nu)^2$   
251  $= 0$ , as shown in Fig. 5 and by assuming the phenomenon of direct transition. The band gap  
252 of  $0.05\text{Sn}_3\text{O}_4/\text{SnS}_2$  NCs,  $0.07\text{Sn}_3\text{O}_4/\text{SnS}_2$  NCs, and  $0.10\text{Sn}_3\text{O}_4/\text{SnS}_2$  NCs were determined to  
253 be 2.23 eV, 2.24 eV and 2.25 eV, respectively, which were similar to that of  $\text{SnS}_2$   
254 nanoclusters ( $E_g = 2.20$  eV).

## 255 **Photocatalytic performance**

256 The photocatalytic reduction of Cr (VI) (50 mg/L) by the batches of  $\text{Sn}_3\text{O}_4/\text{SnS}_2$   
257 nanocomposites (e.g.,  $0.05\text{Sn}_3\text{O}_4/\text{SnS}_2$  NCs,  $0.07\text{Sn}_3\text{O}_4/\text{SnS}_2$  NCs, and  $0.10\text{Sn}_3\text{O}_4/\text{SnS}_2$  NCs)  
258 and those by the individual components, e.g.,  $\text{SnS}_2$  nanoclusters and  $\text{Sn}_3\text{O}_4$  nanoflakes are  
259 given as a plot of  $C_t/C_0$  versus time (Fig. 6a). Here  $C_0$  and  $C_t$  are the initial concentration and  
260 concentration of Cr (VI) after a definite time of sunlight exposure. The decrease in the  
261 concentration of Cr (VI) due to adsorption on the respective photocatalysts was first  
262 determined from the dark experiment. About 40% of Cr (VI) was adsorbed on the batches of  
263 nanocomposites (i.e.,  $0.05\text{Sn}_3\text{O}_4/\text{SnS}_2$  NCs,  $0.07\text{Sn}_3\text{O}_4/\text{SnS}_2$  NCs, and  $0.10\text{Sn}_3\text{O}_4/\text{SnS}_2$  NCs)  
264 while about 14% of Cr (VI) was adsorbed on  $\text{SnS}_2$  nanoclusters and  $\text{Sn}_3\text{O}_4$  nanoflakes (Fig.  
265 6a). The higher adsorption of Cr (VI) is primarily attributable to larger surface area and more  
266 favourable pore volume in  $\text{Sn}_3\text{O}_4/\text{SnS}_2$  NCs (i.e.,  $60.44 \text{ m}^2 \text{ g}^{-1}$ ) as compared to  $55.06 \text{ m}^2 \text{ g}^{-1}$  for  
267 pristine  $\text{SnS}_2$  nanoclusters. As  $\text{Sn}_3\text{O}_4$  fraction was very less in the nanocomposites so its  
268 comparison was not done. The control experiment indicates that the self-decomposition of Cr  
269 (VI) is almost negligible whereas  $\text{Sn}_3\text{O}_4$  shows poor photocatalytic reduction activity after 60

270 min sunlight irradiation. All the batches of Sn<sub>3</sub>O<sub>4</sub>/SnS<sub>2</sub> nanocomposites clearly displayed  
271 significantly higher photocatalytic reduction activity than that of pure SnS<sub>2</sub> after the 60 min  
272 sunlight exposure, which indicates that Sn<sub>3</sub>O<sub>4</sub> plays an important role in the enhancement of  
273 Cr (VI) reduction. The 0.07Sn<sub>3</sub>O<sub>4</sub>/SnS<sub>2</sub> NCs manifested the highest photocatalytic activity  
274 (about 100 % removal efficiency of Cr (VI) after 60 min sunlight irradiations), while only 66  
275 % of Cr (VI) was reduced under same condition using SnS<sub>2</sub> as photocatalyst. Furthermore, it  
276 may be remarked here that the photocatalytic reduction of Cr (VI) by Sn<sub>3</sub>O<sub>4</sub>/SnS<sub>2</sub> NCs are  
277 depend on the content of Sn<sub>3</sub>O<sub>4</sub> in Sn<sub>3</sub>O<sub>4</sub>/SnS<sub>2</sub> NCs. The photocatalytic reduction activity of  
278 0.07Sn<sub>3</sub>O<sub>4</sub>/SnS<sub>2</sub> NCs reached the highest. However, 0.10Sn<sub>3</sub>O<sub>4</sub>/SnS<sub>2</sub> NCs displayed a  
279 decrease in photocatalytic reduction activity, when the Sn<sub>3</sub>O<sub>4</sub> content was further increased.  
280 The most possible reason for the decrease in photocatalytic reduction activity of  
281 0.10Sn<sub>3</sub>O<sub>4</sub>/SnS<sub>2</sub> NCs was that the excess of Sn<sub>3</sub>O<sub>4</sub> covering the active site of Sn<sub>3</sub>O<sub>4</sub>/SnS<sub>2</sub>  
282 NCs, so the number of active sites were reduced. The increase in photocatalytic reduction  
283 activity of 0.07Sn<sub>3</sub>O<sub>4</sub>/SnS<sub>2</sub> can be substantiated with the increase in surface area and pore  
284 volume (as observed in BET results, Table-S2), help in better absorptivity of the Cr (VI)  
285 molecules on the photocatalyst surface as well as formation of heterojunctions in the  
286 Sn<sub>3</sub>O<sub>4</sub>/SnS<sub>2</sub> NCs significantly assist in interfacial charge separation of the photoexcited  
287 excitons during the course of photocatalytic reduction process.

288 The photocatalytic reduction mechanism was studied by fitting the time dependent Cr (VI)  
289 duction data with pseudo first-order kinetics model. The first order kinetics model is  
290 given as:

$$291 \quad \ln(C_0/C_t) = k_1 t \quad (1)$$

292 where,  $C_0$  and  $C_t$  are already defined,  $k_1$  ( $\text{min}^{-1}$ ) is the first order photocatalytic reduction rate  
293 constant for Cr (VI). (Table-1) The corresponding photocatalytic reduction rate of  
294 0.07Sn<sub>3</sub>O<sub>4</sub>/SnS<sub>2</sub> ( $k_1 = 0.066 \text{ min}^{-1}$ ) is 5.5 times than pristine SnS<sub>2</sub> ( $k = 0.012 \text{ min}^{-1}$ ) and 66

295 times with respect to Sn<sub>3</sub>O<sub>4</sub> (k=0.0010 min<sup>-1</sup>, Fig.6b). The corresponding UV-vis absorption  
 296 spectra recorded during the photocatalytic reduction of Cr (VI) solution by the optimized  
 297 0.07Sn<sub>3</sub>O<sub>4</sub>/SnS<sub>2</sub> photocatalyst under sunlight irradiation is given as Supporting Information  
 298 (Fig.S3a). It can be seen that the intensity of the characteristic absorption peak of Cr (VI) at  
 299 about 540 nm decreased gradually and it nearly disappeared after 60 min. Additionally, the  
 300 solution after the photocatalytic reduction of Cr (VI) over 0.07Sn<sub>3</sub>O<sub>4</sub>/SnS<sub>2</sub> sample was  
 301 detected using ICP-OES with Cr (VI) standard curve to confirm the content of Cr ions in  
 302 solution (Fig.S4). The results show that the contents of Cr ions are 0.037 mg/L for sunlight  
 303 light-driven photocatalytic reduction of Cr (VI).

### 304 **Effects of pH on photocatalytic reduction of Cr (VI)**

305 The Cr (VI) removal efficiency continuously decreased with the increasing pH of the  
 306 initial solution. When the pH was increased to 10.50, the total removal rate of Cr (VI) was  
 307 considerably reduced to 14.91%. These results are also presented in the corresponding UV-  
 308 vis absorption spectra (Fig.S5). The higher reduction potential at acidic conditions indicates  
 309 that the reaction is more feasible under acidic conditions. The reasons for the above results  
 310 are as follows. First, Cr (VI) exists mainly as dichromate anion (Cr<sub>2</sub>O<sub>7</sub><sup>2-</sup>) and hydrogen  
 311 chromate ion (HCrO<sub>4</sub><sup>-</sup>) under acidic conditions and as chromate ion (CrO<sub>4</sub><sup>2-</sup>) under alkaline  
 312 conditions. Secondly, under acidic condition, the reduction potential (E Cr<sub>2</sub>O<sub>7</sub><sup>2-</sup>/Cr<sup>3+</sup>) is 1.23  
 313 V vs NHE and (E HCrO<sub>4</sub><sup>-</sup>/Cr<sup>3+</sup>) is 1.35 V vs NHE which is much more positive than the  
 314 reduction potential under alkaline condition i.e. (E CrO<sub>4</sub><sup>2-</sup>/Cr<sup>3+</sup> = -0.13V vs NHE), so  
 315 tendency to reduce from Cr<sup>6+</sup> to Cr<sup>3+</sup> under acidic condition is much more easier than alkaline  
 316 condition (Equation 2-4). The reactions that occur in acidic and alkaline solutions are:

#### 317 **Cr reduction under acidic medium**



320

321 **Cr reduction under alkaline medium**

322



324

325 Overall, the photocatalytic reduction of Cr (VI) consumes  $\text{H}^+$  and acidic conditions are more  
326 favorable for Cr (VI) reduction than basic one.

327 **Photocatalytic degradation of methylene blue (MB) dye**

328 The photocatalytic degradation of another class of pollutants with different molecular  
329 structure, i.e., methylene blue (MB, 20 mg/L) was investigated by all the batches of  
330  $0.07\text{Sn}_3\text{O}_4/\text{SnS}_2$  NCs and those by  $\text{Sn}_3\text{O}_4$  and  $\text{SnS}_2$  NCs. The photocatalytic degradation  
331 profile including the initial dark experiments for MB by all the batches of photocatalysts  
332 under study are given in Fig. 6c. The  $0.07\text{Sn}_3\text{O}_4/\text{SnS}_2$  nanocomposite shows 36% adsorption  
333 of MB dye in the dark condition, whereas  $\text{Sn}_3\text{O}_4$  and  $\text{SnS}_2$  shows 11 % and 13 % adsorption  
334 respectively, indicating that high adsorption capacity favors in the photocatalytic process. As  
335 expected, the sunlight mediated MB degradation was significantly higher for the batches of  
336  $\text{Sn}_3\text{O}_4/\text{SnS}_2$  NCs as compared to those by  $\text{Sn}_3\text{O}_4$  and  $\text{SnS}_2$ . The best result, i.e., 99.6 %  
337 degradation of MB was recorded for the batch treated with  $0.07\text{Sn}_3\text{O}_4/\text{SnS}_2$  NCs. The  
338 degradation followed pseudo-first order kinetic model (Fig. 6d). The corresponding  
339 photocatalytic degradation rate for  $0.07\text{Sn}_3\text{O}_4/\text{SnS}_2$  ( $k_2 = 0.043 \text{ min}^{-1}$ ), which is 5.37 times  
340 higher than the pristine  $\text{SnS}_2$  ( $k = 0.008 \text{ min}^{-1}$ ) and 10.75 times higher than  $\text{Sn}_3\text{O}_4$  ( $k = 0.004$   
341  $\text{min}^{-1}$ ). The corresponding UV-vis absorption spectra recorded during the photocatalytic  
342 degradation of MB dye solution by the optimized  $0.07\text{Sn}_3\text{O}_4/\text{SnS}_2$  photocatalyst under  
343 sunlight irradiation is given as Supporting Information (Fig.S3b). It can be seen that the

344 intensity of the characteristic absorption peak of MB at about 665 nm decreased gradually  
345 and it nearly disappeared after 90 min.

346 The degree of mineralization of MB dye was estimated from total organic content  
347 (TOC) in the respective residual solutions treated with 0.07Sn<sub>3</sub>O<sub>4</sub>/SnS<sub>2</sub> NCs after  
348 photocatalytic degradation for 90 minutes sunlight exposure. Expectedly, these values were  
349 high then the TOC removal by pristine SnS<sub>2</sub> and Sn<sub>3</sub>O<sub>4</sub> (supporting information Fig. S6). The  
350 TOC values were 85.1 % for MB dye, which corresponded to 99.6 % degradation  
351 respectively. Similar trend on incomplete degradation from TOC results are also found in  
352 literature (Du et al. 2021). It may be assumed that longer sunlight exposure could lead to  
353 complete mineralization of MB dye into CO<sub>2</sub> and H<sub>2</sub>O by treating with the photocatalyst (Liu  
354 et al. 2020).

355 The pathways for photocatalytic degradation of MB were addressed by identifying the  
356 tentative intermediates (represented as P) corresponding to the mass fragments analyzed by  
357 UPLC-Q-ToF-MS (Scheme 1).

358 In case of MB, two possible degradation pathways were proposed. On the one  
359 pathway, after a series of demethylation, the structure of MB dye ( $m/z=284$ ) were destroyed  
360 and the intermediates P1 ( $m/z = 255$ ) were appeared. This can be explained that hydroxyl  
361 radicals ( $\cdot\text{OH}$ ) facilitates demethylation of the organic compounds. The intermediate P1 is  
362 further demethylated and deaminized to form intermediate P2 ( $m/z= 198$ ), which was further  
363 oxidised to form intermediate P3 with ( $m/z= 214$ ). The intermediates P3 finally oxidized to  
364 smaller molecule like H<sub>2</sub>O, CO<sub>2</sub>. In the second pathway the sulphur-nitrogen conjugated  
365 system in the MB molecule is attacked by hydroxyl radical and degraded into intermediate P4  
366 ( $m/z= 166$ ). The intermediate P4 undergoes a series of demethylation to form intermediate P5  
367 ( $m/z= 151$ ) and P6 ( $m/z= 138$ ), which was further oxidised to form intermediate P7 with  
368 ( $m/z= 126$ ) and P8 ( $m/z= 109$ ). Now the intermediate P8 undergoes further oxidation and

369 form a smaller molecule i.e., P9 with ( $m/z= 97$ ). In the end, small molecules P9 were further  
370 oxidized into carbon dioxide and water.

### 371 **Re-usability of photocatalyst**

372 The robustness of the as-synthesized batch of  $0.07\text{Sn}_3\text{O}_4/\text{SnS}_2$  NCs as photocatalyst  
373 was assessed from its chemical and photo-stability. The chemical stability was determined  
374 from metal ion leaching during the photocatalytic degradation process. The concentrations of  
375 leached metal ions of Sn at the end of five photocatalytic cycle, determined by calibration  
376 method using ICP-OES analysis, suggested minimal leaching (less than 7 %), as given in  
377 Supporting information Table S3). The concentrations of the leached metal ions in the  
378 reaction medium were determined from the respective calibration plots (Fig. S7). These  
379 results suggested excellent chemical stability of  $0.07\text{Sn}_3\text{O}_4/\text{SnS}_2$  NCs as photocatalyst.

380 The photo-stability of  $0.07\text{Sn}_3\text{O}_4/\text{SnS}_2$  NCs as photocatalyst for Cr (VI)  
381 photoreduction is reflected from the re-usability of the photocatalyst for at least five  
382 successive cycles of photocatalytic reduction under optimized conditions. The photoreduction  
383 patterns are similar and the rate of photocatalytic reduction for all the five cycles are nearly  
384 similar (Fig. 7a). The stability of  $0.07\text{Sn}_3\text{O}_4/\text{SnS}_2$  NCs in the reaction medium was further  
385 confirmed from the XRD pattern of the used photocatalyst recovered after the 5<sup>th</sup> cycle (Fig.  
386 7b). The lattice parameters of the used photocatalyst are expectedly similar (Table S4, given  
387 as Supporting information). Furthermore, the morphology of the used  $0.07\text{Sn}_3\text{O}_4/\text{SnS}_2$  NCs  
388 recorded by FE-SEM also did not show any significant changes with respect to the pristine  
389 batch of photocatalyst (Fig. 7c).

### 390 **Photocatalytic reaction mechanism**

391 Broadly, photocatalytic reduction or degradation is initiated by absorption of photons  
392 of energy greater than the band gap of the photocatalyst followed by inhibition of charge  
393 carrier recombination (Sharma and Dutta 2018). Various factors are responsible for inhibition

394 of charge carrier recombination, out of which the two significant ones are presence of defect  
395 states of energy lesser than that of the conduction band and mobility of charge carriers to the  
396 surface of the photocatalyst for ROS generation.

397 The photoluminescence spectra of pristine  $\text{Sn}_3\text{O}_4$  nanoflakes  $\text{SnS}_2$  nanopartilces,  
398  $0.05\text{Sn}_3\text{O}_4/\text{SnS}_2$  NCs,  $0.07\text{Sn}_3\text{O}_4/\text{SnS}_2$  NCs, and  $0.10\text{Sn}_3\text{O}_4/\text{SnS}_2$  NCs revealed one radiative  
399 transitions, which corresponding to inter-band transition ( $\sim 460$  nm) (Fig. 8a) (Sharma and  
400 Dutta 2018). Notably, the PL emission intensities for inter-band transition were significantly  
401 decreased for the batch of  $\text{Sn}_3\text{O}_4/\text{SnS}_2$  NCs as compared to that of  $\text{Sn}_3\text{O}_4$  and  $\text{SnS}_2$ . The  
402 decrease in the PL intensity is consistent with increase in the rate of photocatalytic reduction  
403 and degradation. These results indicated that the charge carrier recombination is inhibited in  
404  $\text{Sn}_3\text{O}_4/\text{SnS}_2$  and favoured interfacial charge transfer due to formation of heterojunction. These  
405 separated charge carriers have to move to the surface of the photocatalyst for generating  
406 reactive oxygen species (ROS) reacting with molecular oxygen and water. The mobility of  
407 the charge carriers in  $\text{SnS}_2$  and  $\text{Sn}_3\text{O}_4/\text{SnS}_2$  NCs along with was studied from electrochemical  
408 impedance spectroscopy (EIS) measurements. The radius of the arc in the Nyquist plot for the  
409 electrode made of  $0.07\text{Sn}_3\text{O}_4/\text{SnS}_2$  was smaller than the one made of  $\text{SnS}_2$  (Fig. 8b). Arc with  
410 smaller radius, i.e.,  $0.07\text{Sn}_3\text{O}_4/\text{SnS}_2$  NC, is attributed to lower the impedance or higher charge  
411 carrier transport (Li et al. 2018b; Yi et al. 2019). Furthermore, the slope in the mid-frequency  
412 region corresponding to the Warburg region is more for  $0.07\text{Sn}_3\text{O}_4/\text{SnS}_2$ , which implied  
413 higher diffusion current than in pristine  $\text{SnS}_2$ . These results are consistent with more  
414 favourable charge carrier transport in  $0.07\text{Sn}_3\text{O}_4/\text{SnS}_2$  as compared to the pristine  $\text{SnS}_2$  and  
415 complimented with the higher photocatalytic activity exhibited by observed in  
416  $0.07\text{Sn}_3\text{O}_4/\text{SnS}_2$ .

417 The interfacial charge transfer in a heterogeneous photocatalyst would depend on  
418 favourable configuration of conduction band and valence band energies in the photocatalyst.

419 Empirically, the minimum energy of conduction band ( $E_{CB}$ ) and the maximum energy of the  
420 valence band ( $E_{VB}$ ) were calculated by using the following expressions: (Reddy et al. 1998)

$$421 \quad E_{CB} = \chi(A_aB_b) - 1/2E_g + E_o \quad (5)$$

$$422 \quad E_{VB} = E_{CB} + E_g \quad (6)$$

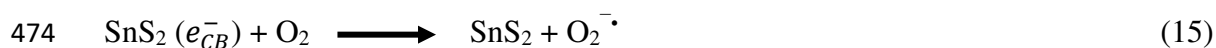
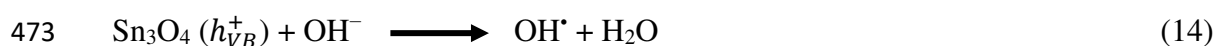
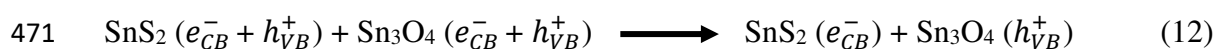
423 where,  $E_g$  is the band gap of  $0.07\text{Sn}_3\text{O}_4/\text{SnS}_2$  NCs,  $E_{CB}$  is the potential of the conduction  
424 band,  $E_{VB}$  is the valence band potential,  $E_o$  is the scale factor taken as  $-4.50$  eV, *i.e.*, the  
425 energy of free electrons on the normal hydrogen electrode (NHE scale). The  
426 parameter  $\chi(A_aB_b)$  corresponds to the absolute electronegativity of a semiconductor material  
427 type  $A_aB_b$ , which is calculated as the geometric mean of the electronegativity of the  
428 constituent atoms. The electronegativity value for  $\text{Sn}_3\text{O}_4$  and  $\text{SnS}_2$  are calculated to be  $5.91$   
429 eV and  $5.37$  eV, respectively, which are consistent with literature (Gao et al. 2016; Li et al.  
430 2018a). The  $E_{CB}$  and  $E_{VB}$  of  $\text{Sn}_3\text{O}_4$  are deduced as  $0.01$  eV and  $2.81$  eV, respectively.  
431 Similarly, the  $E_{CB}$  and the  $E_{VB}$  of  $\text{SnS}_2$  are  $-0.11$  eV and  $2.09$  eV, respectively. Since the  
432 conduction band potential of  $\text{SnS}_2$  is more negative than that of  $\text{Sn}_3\text{O}_4$ , the photogenerated  
433 electrons in the conduction band of  $\text{SnS}_2$  will migrate to the conduction band of  $\text{Sn}_3\text{O}_4$ ,  
434 according to the traditional separation process of electron-hole pairs (Luo et al. 2019). By this  
435 charge transfer mode, the accumulated electrons in the conduction band of  $\text{Sn}_3\text{O}_4$  cannot  
436 reduce  $\text{O}_2$  into  $\text{O}_2^{\cdot-}$  radicals because the conduction band potential of  $\text{Sn}_3\text{O}_4$  is more positive  
437 than that of the  $\text{O}_2^{\cdot-}$  radical ( $-0.046$  eV vs N.H.E) (Li et al. 2018a). Thus, it is not favourable  
438 for producing the main reactive species  $\text{O}_2^{\cdot-}$  if transfer of photogenerated charge occurs by  
439 the traditional electron-hole transfer process. However, the results of this trapping  
440 experiments revealed that  $\text{O}_2^{\cdot-}$  play an important role in the organic pollutant degradation  
441 process. On the basis of the above results, a possible Z-scheme mechanism for Cr (VI)  
442 reduction and MB degradation using the  $\text{Sn}_3\text{O}_4/\text{SnS}_2$  heterojunction photocatalyst was  
443 proposed, as illustrated in scheme-2a and 2b. Unlike the traditional model, the Z-scheme

444 mechanism photocatalysts retain the stronger oxidation and reduction ability, which deeply  
 445 contributed to the improvement of photocatalytic performance (Liu et al. 2018; Lin et al.  
 446 2021; Qiang et al. 2021). Under visible-light irradiation, both SnS<sub>2</sub> and Sn<sub>3</sub>O<sub>4</sub> can absorb  
 447 visible light photons to produce photogenerated electrons and holes. In case Cr (VI)  
 448 photoreduction (scheme-2a), the photogenerated electrons in conduction band of Sn<sub>3</sub>O<sub>4</sub> ( $e_{CB}^-$ )  
 449 would transfer to valence band of SnS<sub>2</sub> to recombine instantly with the photogenerated holes  
 450 ( $h_{VB}^+$ ), while the valence band holes of Sn<sub>3</sub>O<sub>4</sub> incite the decomposition of water with the  
 451 photo-oxidation reaction. On the other hand, the conduction band electrons of SnS<sub>2</sub> could  
 452 easily utilize for the reduction of Cr (VI) to Cr (III), as the potential of conduction band of  
 453 SnS<sub>2</sub> (-0.11 eV) is more negative than the potential required for Cr (VI) photoreduction  
 454 ( $E(\text{Cr}^{6+}/\text{Cr}^{3+}) = 0.55 \text{ eV vs. NHE}$ ). The pathways of Cr (VI) reduction are depicted in Eqs. (7-  
 455 9).



459 The possible photocatalytic degradation mechanism of MB by Sn<sub>3</sub>O<sub>4</sub>/SnS<sub>2</sub> NCs is shown in  
 460 (Scheme 2b). By analyzing the relative band gap positions of  $E_{CB}$  and the  $E_{VB}$  of SnS<sub>2</sub> and  
 461 Sn<sub>3</sub>O<sub>4</sub>, it can be found that the thermodynamic driving force of  $e^-$  in conduction band of SnS<sub>2</sub>  
 462 is enough to reduce the adsorbed oxygen to generate  $\text{O}_2^{\cdot-}$  ( $E(\text{O}_2/\text{O}_2^{\cdot-}) = -0.046 \text{ eV vs.}$   
 463 NHE). Meanwhile, the lower valence band potentials of Sn<sub>3</sub>O<sub>4</sub> (2.81 eV) instead of SnS<sub>2</sub>  
 464 (2.09 eV) can oxidize  $\text{OH}^-$  to  $\text{OH}^{\cdot}$  owing to the standard redox potential of  $\text{OH}^{\cdot}/\text{OH}^-$  with 2.3  
 465 eV. Therefore, it is clear that in this heterojunction system,  $\text{O}_2^{\cdot-}$  and  $\text{OH}^{\cdot}$  are the mainstream  
 466 active sites who truly matter in this photocatalytic degradation reaction.

467 This is well supported by the radical trapping studies (Fig. 9c), and the photogenerated charge  
 468 carrier transfer process can be described as follows:



477 Consequently conclusion can be drawn that the photo-degradation by  $\text{Sn}_3\text{O}_4/\text{SnS}_2$   
 478 heterojunctions followed a direct Z-scheme mechanism, which not only promotes the  
 479 separation efficiency of photogenerated electrons and holes but also shows a strong redox  
 480 ability for antibiotic degradation.

### 481 **Reactive oxygen species (ROS) scavenging studies**

482 The influence of in-situ generated ROS in the reaction medium towards degradation  
 483 of MB has been explored from some of the specific ROS scavenging action. The discussion  
 484 in the previous section strongly indicated the role of superoxide radicals ( $\text{O}_2^{\bullet -}$ ) towards  
 485 photocatalytic degradation of MB by the optimum performing batch of  $0.07\text{Sn}_3\text{O}_4/\text{SnS}_2$ . In  
 486 this pursuit, the hydroxide radicals ( $\bullet\text{OH}$ ) are expected to play important role. Apart from  
 487 this, generation of superoxide radicals ( $\text{O}_2^{\bullet -}$ ) is relevant when photoexcited electrons are  
 488 involved during photocatalytic process. In view of this photocatalytic degradation of MB by  
 489  $0.07\text{Sn}_3\text{O}_4/\text{SnS}_2$  NCs was monitored under optimized conditions in the presence of specific  
 490 ROS scavengers, e.g. isopropyl alcohol (IPA, 1 mM) for scavenging  $\text{OH}^\bullet$  radicals (Sharma et  
 491 al. 2017); ammonium oxalate (AO, 1 mM) for scavenging  $h^+$  (Sharma and Dutta 2015); and  
 492 chloroform (1 mM) for scavenging  $\text{O}_2^{\bullet -}$  (Mukherjee et al. 2021) radical, respectively. The  
 493 ROS scavenging action was evident from the decrease in the rate of photocatalytic

494 degradation of MB (Fig. 8c). The most significant decrease in the rate of photocatalytic  
495 degradation of MB was observed for the batch treated with chloroform, i.e., super oxide  
496 radical scavenger (Table S5). This strongly suggested that the super oxide radical played very  
497 important role in the photocatalytic degradation of MB by 0.07Sn<sub>3</sub>O<sub>4</sub>/SnS<sub>2</sub> photocatalyst.  
498 Besides, the decrease in the rate of photocatalytic degradation of MB by 0.07Sn<sub>3</sub>O<sub>4</sub>/SnS<sub>2</sub> in  
499 the presence of isopropyl alcohol (OH<sup>•</sup> radicals scavenger) suggested that the photoexcited  
500 holes were also involved in generating ROS in the reaction medium. The ROS scavenging  
501 studies complimented the PL results of 0.07Sn<sub>3</sub>O<sub>4</sub>/SnS<sub>2</sub> regarding predominant generation of  
502 super oxide radicals due to inhibition photoexcited charge carriers for the batch of  
503 0.07Sn<sub>3</sub>O<sub>4</sub>/SnS<sub>2</sub> NC and consequential enhanced photocatalytic degradation of MB.

504 It may be concluded that Sn<sub>3</sub>O<sub>4</sub>/SnS<sub>2</sub> nanocomposites are excellent solar photocatalyst  
505 which can be used for photoreduction of Cr (VI) and degradation of MB without any  
506 exogenous oxidant, e.g., ozone or hydrogen peroxide. It also does not require any electricity  
507 for operation. Further studies needs to be done to check its efficiency in real time tertiary  
508 treatment in water treatment plants.

## 509 **Conclusion**

510 A novel photocatalyst, *viz.* Sn<sub>3</sub>O<sub>4</sub>/SnS<sub>2</sub> nanocomposite has been synthesized by a  
511 simple two-step hydrothermal synthetic route, which exhibited enhanced photocatalytic  
512 activity than its constituents towards photoreduction of hexavalent chromium Cr (VI) and  
513 degradation of methylene blue (MB) under natural sunlight. The rate constant for  
514 photocatalytic reduction and degradation of Cr (VI) and MB, respectively, by  
515 0.07Sn<sub>3</sub>O<sub>4</sub>/SnS<sub>2</sub> were about five times higher than that of SnS<sub>2</sub> photocatalyst. The improved  
516 rate constant has been discussed in the light of separation of the photogenerated charge  
517 carriers owing to formation of a Z-scheme heterojunction and sustained release of reactive  
518 oxygen species in the reaction medium. The photocatalytic degradation mechanism has been

519 addressed by analyzing the degradation product by UPLC-Q-ToF-MS and from total carbon  
520 content. The excellent chemical and photostability and re-usability of Sn<sub>3</sub>O<sub>4</sub>/SnS<sub>2</sub>  
521 nanocomposite, makes it an efficient photocatalyst choice for the potential degradation of  
522 organic compounds in wastewater.

## 523 **Statements and Declarations**

524 **Funding information** Fund not available for this work.

525 **Competing Interest** The authors declare no competing interests

526 **Ethics approval** Not applicable

527 **Consent to participate** Not applicable

528 **Consent for publication** Not applicable

529 **Authors contributions** Gandharve Kumar contributed to the study conception and design  
530 and experiments. R.K. Dutta supervised the work and prepared the manuscript.

531

## 532 **References**

533 Barrera-Díaz CE, Lugo-Lugo V, Bilyeu B (2012) A review of chemical, electrochemical and  
534 biological methods for aqueous Cr (VI) reduction. *J Hazard Mater* 223–224:1–12.  
535 <https://doi.org/10.1016/j.jhazmat.2012.04.054>

536 Bethi B, Sonawane SH, Bhanvase BA, Gumfekar SP (2016) Nanomaterials-based advanced  
537 oxidation processes for wastewater treatment: A review. *Chem Eng Process Process*  
538 *Intensif* 109:178–189. <https://doi.org/10.1016/j.cep.2016.08.016>

539 Calvete MJF, Piccirillo G, Vinagreiro CS, Pereira MM (2019) Hybrid materials for  
540 heterogeneous photocatalytic degradation of antibiotics. *Coord Chem Rev* 395:63–85.  
541 <https://doi.org/10.1016/j.ccr.2019.05.004>

542 Coetzee JJ, Bansal N, Chirwa EMN (2020) Chromium in Environment, Its Toxic Effect from

543 Chromite-Mining and Ferrochrome Industries, and Its Possible Bioremediation. *Expo*  
544 *Heal* 12:51–62. <https://doi.org/10.1007/s12403-018-0284-z>

545 Das D, Dutta RK (2015) A novel method of synthesis of small band gap SnS nanorods and its  
546 efficient photocatalytic dye degradation. *J Colloid Interface Sci* 457:339–344.  
547 <https://doi.org/10.1016/j.jcis.2015.07.002>

548 Di T, Xu Q, Ho WK, et al (2019) Review on Metal Sulphide-based Z-scheme Photocatalysts.  
549 *ChemCatChem* 11:1394–1411. <https://doi.org/10.1002/cctc.201802024>

550 Du Z, Feng L, Guo Z, et al (2021) Ultrathin h-BN/Bi<sub>2</sub>MoO<sub>6</sub> heterojunction with synergetic  
551 effect for visible-light photocatalytic tetracycline degradation. *J Colloid Interface Sci*  
552 589:545–555. <https://doi.org/10.1016/j.jcis.2021.01.027>

553 Fick J, Söderström H, Lindberg RH, et al (2009) Pharmaceuticals and personal care products  
554 in the environment contamination of surface, ground, and drinking water from  
555 pharmaceutical production. *Environ Toxicol Chem* 28:2522–2527

556 Gao X, Huang G, Gao H, et al (2016) Facile fabrication of Bi<sub>2</sub>S<sub>3</sub>/SnS<sub>2</sub> heterojunction  
557 photocatalysts with efficient photocatalytic activity under visible light. *J Alloys Compd*  
558 674:98–108. <https://doi.org/10.1016/j.jallcom.2016.03.031>

559 Gusain R, Gupta K, Joshi P, Khatri OP (2019) Adsorptive removal and photocatalytic  
560 degradation of organic pollutants using metal oxides and their composites: A  
561 comprehensive review. *Adv Colloid Interface Sci* 272:102009.  
562 <https://doi.org/10.1016/j.cis.2019.102009>

563 Hafiane A, Lemordant D, Dhahbi M (2000) Removal of hexavalent chromium by  
564 nanofiltration. *Desalination* 130:305–312. [https://doi.org/10.1016/S0011-](https://doi.org/10.1016/S0011-9164(00)00094-1)  
565 [9164\(00\)00094-1](https://doi.org/10.1016/S0011-9164(00)00094-1)

566 He C, Gu L, Xu Z, et al (2020) Cleaning chromium pollution in aquatic environments by  
567 bioremediation, photocatalytic remediation, electrochemical remediation and coupled  
568 remediation systems. *Environ Chem Lett* 18:561–576. [https://doi.org/10.1007/s10311-](https://doi.org/10.1007/s10311-019-00960-3)  
569 [019-00960-3](https://doi.org/10.1007/s10311-019-00960-3)

570 Huang D, Li J, Zeng G, et al (2019) Facile construction of hierarchical flower-like Z-scheme  
571 AgBr/Bi<sub>2</sub>WO<sub>6</sub> photocatalysts for effective removal of tetracycline: Degradation  
572 pathways and mechanism. *Chem Eng J* 375:121991.  
573 <https://doi.org/10.1016/j.cej.2019.121991>

574 Karimi-Maleh H, Ayati A, Ghanbari S, et al (2021) Recent advances in removal techniques  
575 of Cr (VI) toxic ion from aqueous solution: A comprehensive review. *J Mol Liq* 329:.  
576 <https://doi.org/10.1016/j.molliq.2020.115062>

577 Katheresan V, Kansedo J, Lau SY (2018) Efficiency of various recent wastewater dye  
578 removal methods: A review. *J Environ Chem Eng* 6:4676–4697.  
579 <https://doi.org/10.1016/j.jece.2018.06.060>

580 Khan NA, Ahmed S, Farooqi IH, et al (2020) Occurrence, sources and conventional  
581 treatment techniques for various antibiotics present in hospital wastewaters: A critical  
582 review. *TrAC - Trends Anal Chem* 129:.  
<https://doi.org/10.1016/j.trac.2020.115921>

583 Khatri A, Peerzada MH, Mohsin M, White M (2015) A review on developments in dyeing  
584 cotton fabrics with reactive dyes for reducing effluent pollution. *J Clean Prod* 87:50–57.  
585 <https://doi.org/10.1016/j.jclepro.2014.09.017>

586 Kortüm G (1969) *Reflectance Spectroscopy*, translated by JE Lohr

587 Li C, Yu S, Dong H, et al (2018a) Z-scheme mesoporous photocatalyst constructed by  
588 modification of Sn<sub>3</sub>O<sub>4</sub> nanoclusters on g-C<sub>3</sub>N<sub>4</sub> nanosheets with improved photocatalytic

589 performance and mechanism insight. *Appl Catal B Environ* 238:284–293.  
590 <https://doi.org/10.1016/j.apcatb.2018.07.049>

591 Li H, Hu T, Zhang R, et al (2016) Preparation of solid-state Z-scheme Bi<sub>2</sub>MoO<sub>6</sub>/MO (MCu,  
592 Co<sub>3/4</sub>, or Ni) heterojunctions with internal electric field-improved performance in  
593 photocatalysis. *Appl Catal B Environ* 188:313–323.  
594 <https://doi.org/10.1016/j.apcatb.2016.02.015>

595 Li Z, Meng X, Zhang Z (2018b) Few-layer MoS<sub>2</sub> nanosheets-deposited on Bi<sub>2</sub>MoO<sub>6</sub>  
596 microspheres: A Z-scheme visible-light photocatalyst with enhanced activity. *Catal*  
597 *Today* 315:67–78. <https://doi.org/10.1016/j.cattod.2018.03.014>

598 Lin Z, Zheng Y, Deng F, et al (2021) Target-directed design of dual-functional Z-scheme  
599 AgIn<sub>5</sub>S<sub>8</sub>/SnS<sub>2</sub> heterojunction for Pb(II) capture and photocatalytic reduction of Cr (VI):  
600 Performance and mechanism insight. *Sep Purif Technol* 277:119430.  
601 <https://doi.org/10.1016/j.seppur.2021.119430>

602 Liu C, Lü H, Yu C, et al (2020) Novel FeWO<sub>4</sub>/WO<sub>3</sub> nanoplate with p-n heterostructure and  
603 its enhanced mechanism for organic pollutants removal under visible-light illumination.  
604 *J Environ Chem Eng* 8:104044. <https://doi.org/10.1016/j.jece.2020.104044>

605 Liu Y, Geng P, Wang J, et al (2018) In-situ ion-exchange synthesis Ag<sub>2</sub>S modified SnS<sub>2</sub>  
606 nanosheets toward highly photocurrent response and photocatalytic activity. *J Colloid*  
607 *Interface Sci* 512:784–791. <https://doi.org/10.1016/j.jcis.2017.10.112>

608 Luo J, Li R, Chen Y, et al (2019) Rational design of Z-scheme LaFeO<sub>3</sub>/SnS<sub>2</sub> hybrid with  
609 boosted visible light photocatalytic activity towards tetracycline degradation. *Sep Purif*  
610 *Technol* 210:417–430. <https://doi.org/10.1016/j.seppur.2018.08.028>

611 Mertz W (1993) Chromium in Human Nutrition: A Review. *J Nutr* 123:626–633.

612 <https://doi.org/10.1093/jn/123.4.626>

613 Mukherjee I, Cilamkoti V, Dutta RK (2021) Sunlight-driven photocatalytic degradation of  
614 ciprofloxacin by carbon dots embedded in ZnO nanostructures. *ACS Appl Nano Mater.*  
615 <https://doi.org/10.1021/acsanm.1c00883>

616 Narayani M, Shetty KV (2013) Chromium-resistant bacteria and their environmental  
617 condition for hexavalent chromium removal: A review. *Crit Rev Environ Sci Technol*  
618 43:955–1009. <https://doi.org/10.1080/10643389.2011.627022>

619 Owlad M, Aroua MK, Daud WAW, Baroutian S (2009) Removal of hexavalent chromium-  
620 contaminated water and wastewater: A review. *Water Air Soil Pollut* 200:59–77.  
621 <https://doi.org/10.1007/s11270-008-9893-7>

622 Peng Y, Chen QG, Wang D, et al (2015) Synthesis of one-dimensional  $\text{WO}_3\text{-Bi}_2\text{WO}_6$   
623 heterojunctions with enhanced photocatalytic activity. *CrystEngComm* 17:569–576.  
624 <https://doi.org/10.1039/c4ce01884b>

625 Qiang T, Chen L, Xia Y, Qin X (2021) Dual modified  $\text{MoS}_2/\text{SnS}_2$  photocatalyst with Z-  
626 scheme heterojunction and vacancies defects to achieve a superior performance in Cr  
627 (VI) reduction and dyes degradation. *J Clean Prod* 291:125213.  
628 <https://doi.org/10.1016/j.jclepro.2020.125213>

629 Ramachandra T V., Jain R, Krishnadas G (2011) Hotspots of solar potential in India. *Renew*  
630 *Sustain Energy Rev* 15:3178–3186. <https://doi.org/10.1016/j.rser.2011.04.007>

631 Reddy RR, Nazeer Ahammed Y, Rama Gopal K, Raghuram D V. (1998) Optical  
632 electronegativity and refractive index of materials. *Opt Mater (Amst)* 10:95–100.  
633 [https://doi.org/10.1016/S0925-3467\(97\)00171-7](https://doi.org/10.1016/S0925-3467(97)00171-7)

634 Saadati F, Keramati N, Ghazi MM (2016) Influence of parameters on the photocatalytic

635 degradation of tetracycline in wastewater: A review. *Crit Rev Environ Sci Technol*  
636 46:757–782. <https://doi.org/10.1080/10643389.2016.1159093>

637 Sedman RM, Beaumont J, McDonald TA, et al (2006) Review of the evidence regarding the  
638 carcinogenicity of hexavalent chromium in drinking water. *J Environ Sci Heal - Part C*  
639 *Environ Carcinog Ecotoxicol Rev* 24:155–182.  
640 <https://doi.org/10.1080/10590500600614337>

641 Sharma A, Dutta RK (2018) Se-doped CuO NPs/H<sub>2</sub>O<sub>2</sub>/UV as a highly efficient and  
642 sustainable photo-Fenton catalytic system for enhanced degradation of 4-bromophenol. *J*  
643 *Clean Prod* 185:464–475. <https://doi.org/10.1016/j.jclepro.2018.03.049>

644 Sharma A, Dutta RK (2015) Studies on the drastic improvement of photocatalytic  
645 degradation of acid orange-74 dye by TPPO capped CuO nanoparticles in tandem with  
646 suitable electron capturing agents. *RSC Adv* 5:43815–43823.  
647 <https://doi.org/10.1039/c5ra04179a>

648 Sharma A, Dutta RK, Roychowdhury A, et al (2017) Cobalt doped CuO nanoparticles as a  
649 highly efficient heterogeneous catalyst for reduction of 4-nitrophenol to 4-aminophenol.  
650 *Appl Catal A Gen* 543:257–265. <https://doi.org/10.1016/j.apcata.2017.06.037>

651 Sharma S, Bhattacharya A (2017) Drinking water contamination and treatment techniques.  
652 *Appl Water Sci* 7:1043–1067. <https://doi.org/10.1007/s13201-016-0455-7>

653 Singh R, Singh AP, Kumar S, et al (2019) Antibiotic resistance in major rivers in the world:  
654 A systematic review on occurrence, emergence, and management strategies. *J Clean*  
655 *Prod* 234:1484–1505. <https://doi.org/10.1016/j.jclepro.2019.06.243>

656 Tauc J, Grigorovici R, Vancu A (1966) Optical properties and electronic structure of  
657 amorphous germanium. *Phys status solidi* 15:627–637.

658 <https://doi.org/https://doi.org/10.1002/pssb.19660150224>

659 Tumolo M, Ancona V, De Paola D, et al (2020) Chromium pollution in European water,  
660 sources, health risk, and remediation strategies: An overview. *Int J Environ Res Public*  
661 *Health* 17:1–25. <https://doi.org/10.3390/ijerph17155438>

662 Wang R, Zhu P, Liu M, et al (2021) Synthesis and characterization of magnetic ZnFe<sub>2</sub>O<sub>4</sub>/Bi<sup>0</sup>-  
663 Bi<sub>2</sub>MoO<sub>6</sub> with Z-scheme heterojunction for antibiotics degradation under visible light.  
664 *Sep Purif Technol* 277:119339. <https://doi.org/10.1016/j.seppur.2021.119339>

665 Wang Y, Su Y, Fang W, et al (2020) SnO<sub>2</sub>/SnS<sub>2</sub> nanocomposite anchored on nitrogen-doped  
666 RGO for improved photocatalytic reduction of aqueous Cr(VI). *Powder Technol*  
667 363:337–348. <https://doi.org/10.1016/j.powtec.2020.01.009>

668 Wei Z, Liu J, Shangguan W (2020) A review on photocatalysis in antibiotic wastewater:  
669 Pollutant degradation and hydrogen production. *Chinese J Catal* 41:1440–1450.  
670 [https://doi.org/10.1016/S1872-2067\(19\)63448-0](https://doi.org/10.1016/S1872-2067(19)63448-0)

671 Xu L, Chen W qian, Ke S qiang, et al (2020) Construction of heterojunction Bi/Bi<sub>5</sub>O<sub>7</sub>I/Sn<sub>3</sub>O<sub>4</sub>  
672 for efficient noble-metal-free Z-scheme photocatalytic H<sub>2</sub> evolution. *Chem Eng J*  
673 382:122810. <https://doi.org/10.1016/j.cej.2019.122810>

674 Yaseen DA, Scholz M (2019) Textile dye wastewater characteristics and constituents of  
675 synthetic effluents: a critical review. Springer Berlin Heidelberg

676 Yi J, Mo H, Zhang B, et al (2019) CeO<sub>2</sub>/Bi<sub>2</sub>MoO<sub>6</sub> heterostructured microspheres with  
677 synergistic effect for accelerating photogenerated charge separation. *Sep Purif Technol*  
678 211:474–480. <https://doi.org/10.1016/j.seppur.2018.10.022>

679 Zhang G, Chen D, Li N, et al (2019) Fabrication of Bi<sub>2</sub>MoO<sub>6</sub>/ZnO hierarchical  
680 heterostructures with enhanced visible-light photocatalytic activity. *Appl Catal B*

681 Environ 250:313–324. <https://doi.org/10.1016/j.apcatb.2019.03.055>

682 Zhang H, Bian H, Zhang H, et al (2020) Magnetic Separable Bi<sub>2</sub>Fe<sub>4</sub>O<sub>9</sub>/Bi<sub>2</sub>MoO<sub>6</sub>  
683 Heterojunctions in Z-Scheme with Enhanced Visible-Light Photocatalytic Activity for  
684 Organic Pollutant Degradation. Catal Letters 150:2464–2473.  
685 <https://doi.org/10.1007/s10562-020-03157-4>

686 Zhao W, Feng Y, Huang H, et al (2019) A novel Z-scheme Ag<sub>3</sub>VO<sub>4</sub>/BiVO<sub>4</sub> heterojunction  
687 photocatalyst: Study on the excellent photocatalytic performance and photocatalytic  
688 mechanism. Appl Catal B Environ 245:448–458.  
689 <https://doi.org/10.1016/j.apcatb.2019.01.001>

690

### 691 **Table captions**

692 **Table 1.** Summary of the photocatalytic reduction of Cr (VI) and photocatalytic degradation  
693 of methylene blue experiments carried out under optimized condition, i.e. photocatalyst and  
694 sunlight.

### 695 **Figure Captions.**

### 696 **Figure Captions.**

697 **Fig. 1** XRD patterns of the as-synthesized batches of SnS<sub>2</sub> nanoparticles, Sn<sub>3</sub>O<sub>4</sub> nanoflakes,  
698 0.05Sn<sub>3</sub>O<sub>4</sub>/SnS<sub>2</sub> nanocomposite, 0.07Sn<sub>3</sub>O<sub>4</sub>/SnS<sub>2</sub> nanocomposite, and 0.10Sn<sub>3</sub>O<sub>4</sub>/SnS<sub>2</sub>  
699 nanocomposite.

700 **Fig. 2** Low resolution transmission electron microscopy images of 0.07Sn<sub>3</sub>O<sub>4</sub>/SnS<sub>2</sub> (a-b);  
701 higher resolution transmission electron microscopy images of 0.07Sn<sub>3</sub>O<sub>4</sub>/SnS<sub>2</sub> (c); (d)  
702 selected area electron diffraction pattern of 0.07Sn<sub>3</sub>O<sub>4</sub>/SnS<sub>2</sub>

703 **Fig. 3** Binding energy spectra of 0.07Sn<sub>3</sub>O<sub>4</sub>/SnS<sub>2</sub>nanocomposite obtained from X-ray  
704 photoelectron spectroscopy measurements of (a) survey spectrum; (b) Sn 3d; (c) S 2p; and (d)  
705 O 1s.

706 **Fig. 4** N<sub>2</sub> adsorption- desorption isotherms of pristine SnS<sub>2</sub> and 0.07Sn<sub>3</sub>O<sub>4</sub>/SnS<sub>2</sub> NCs (Inset  
707 represents the respective pore size distribution curves of pristine SnS<sub>2</sub> and 0.07Sn<sub>3</sub>O<sub>4</sub>/SnS<sub>2</sub>  
708 NCs).

709 **Fig. 5** Tauc's plot of pristine Sn<sub>3</sub>O<sub>4</sub>, pristine SnS<sub>2</sub>, and Sn<sub>3</sub>O<sub>4</sub>/SnS<sub>2</sub> composites.

710 **Fig. 6** a) Dynamic curves of photocatalytic reduction of Cr( VI) by different photocatalysts  
711 under sunlight irradiation, b) pseudo first- order kinetic fitting of Cr (VI) reduction over  
712 different photocatalyst under sunlight irradiation, c) Dynamic curves of photocatalytic  
713 degradation of MB by different photocatalysts under sunlight irradiation, and d) pseudo first-  
714 order kinetic fitting of MB degradation over different photocatalyst under sunlight  
715 irradiation, under sunlight.

716 **Fig. 7** (a) Recyclability of the 0.07Sn<sub>3</sub>O<sub>4</sub>/SnS<sub>2</sub> NCs up to five photocatalytic reduction cycles;  
717 (b) X-ray diffraction pattern and (c) scanning electron microscopy image of the recycled  
718 photocatalyst.

719 **Fig. 8** a) Steady state room- temperature photoluminescence (PL) spectra, (b) electrochemical  
720 impedance spectra of SnS<sub>2</sub> and 0.07Sn<sub>3</sub>O<sub>4</sub>/SnS<sub>2</sub>, and, (c) Effect of reactive oxygen species  
721 scavengers on photocatalytic reduction of Cr (VI) by 0.07Sn<sub>3</sub>O<sub>4</sub>/SnS<sub>2</sub> nanocomposites under  
722 sunlight.

723 **Scheme 1** Schematic diagram of proposed MB degradation pathway by 0.07Sn<sub>3</sub>O<sub>4</sub>/SnS<sub>2</sub> NCS  
724 along with MS spectra of possible intermediate of MB photodegradation by 0.07Sn<sub>3</sub>O<sub>4</sub>/SnS<sub>2</sub>.

725 **Scheme 2.** Possible photocatalytic mechanism of Cr (VI) (a) and MB (b) on 0.07Sn<sub>3</sub>O<sub>4</sub>/SnS<sub>2</sub>  
726 nanocomposites

727

**Table 1**

Sample name	% adsorption	% Reduction	1 <sup>st</sup> order kinetics Sunlight (Cr(VI))		% adsorption	% Degradation	1 <sup>st</sup> order kinetics Sunlight (MB)	
			Rate constant (min <sup>-1</sup> )	R <sup>2</sup>			Rate constant (min <sup>-1</sup> )	R <sup>2</sup>
0.10Sn <sub>3</sub> O <sub>4</sub> /SnS <sub>2</sub>	21%	89%	0.032	0.994	33%	91%	0.020	0.989
0.07Sn <sub>3</sub> O <sub>4</sub> /SnS <sub>2</sub>	17%	100%	0.066	0.991	36%	99.6%	0.043	0.996
0.05Sn <sub>3</sub> O <sub>4</sub> /SnS <sub>2</sub>	20%	90%	0.034	0.993	30%	84%	0.015	0.990
SnS <sub>2</sub>	14%	66%	0.012	0.995	13%	58%	0.008	0.991
Sn <sub>3</sub> O <sub>4</sub>	15%	18%	0.0010	0.974	11%	39%	0.004	0.970
Blank	NA	10%	0.002	0.983	NA	9%	0.001	0.975

Figures

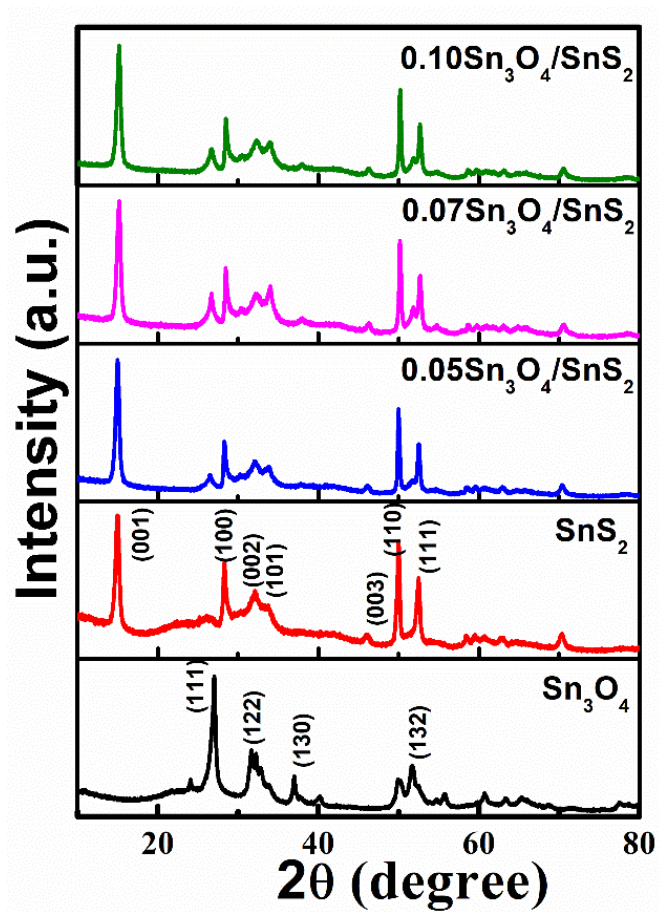


Fig. 1.

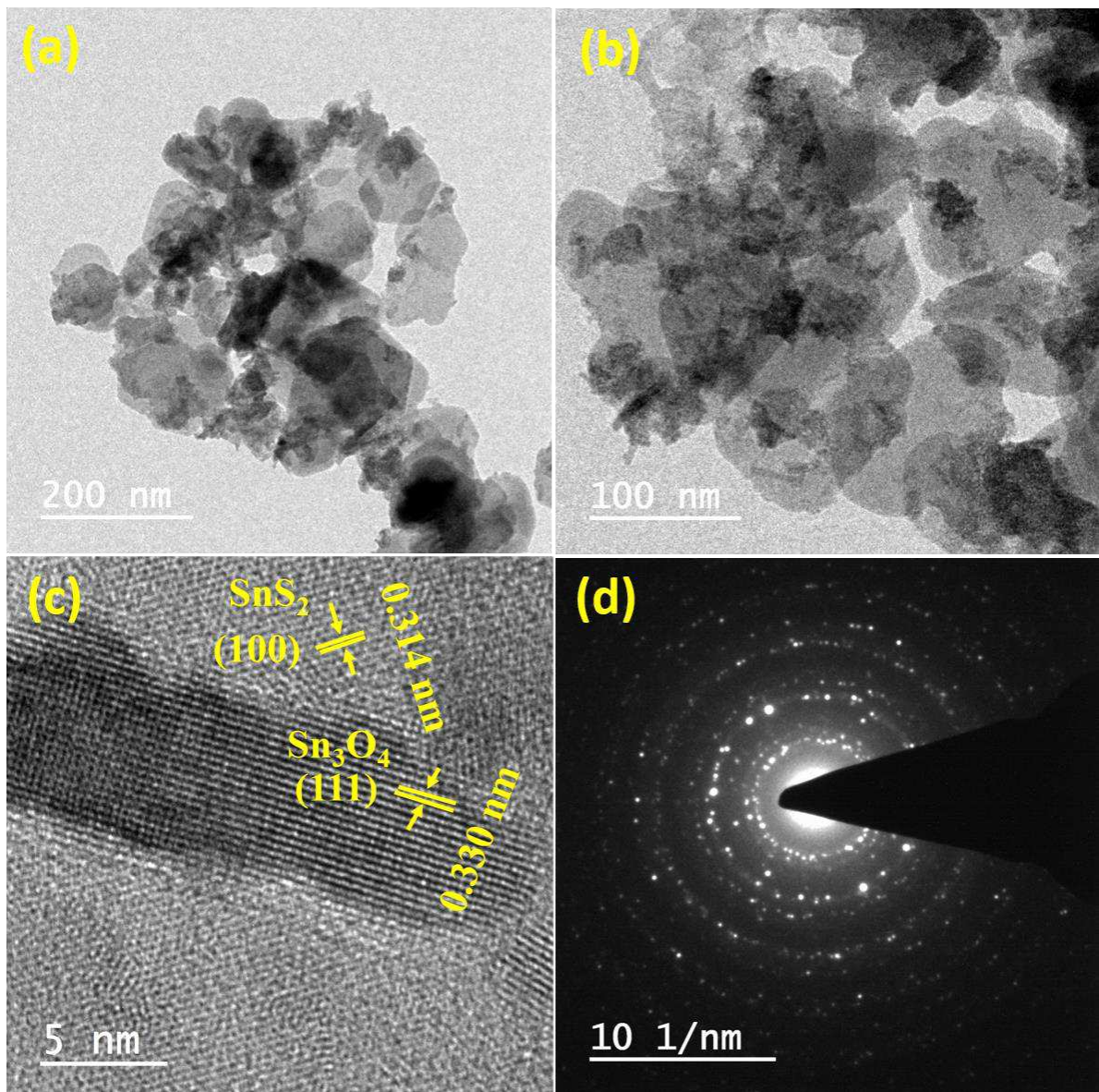


Fig. 2.

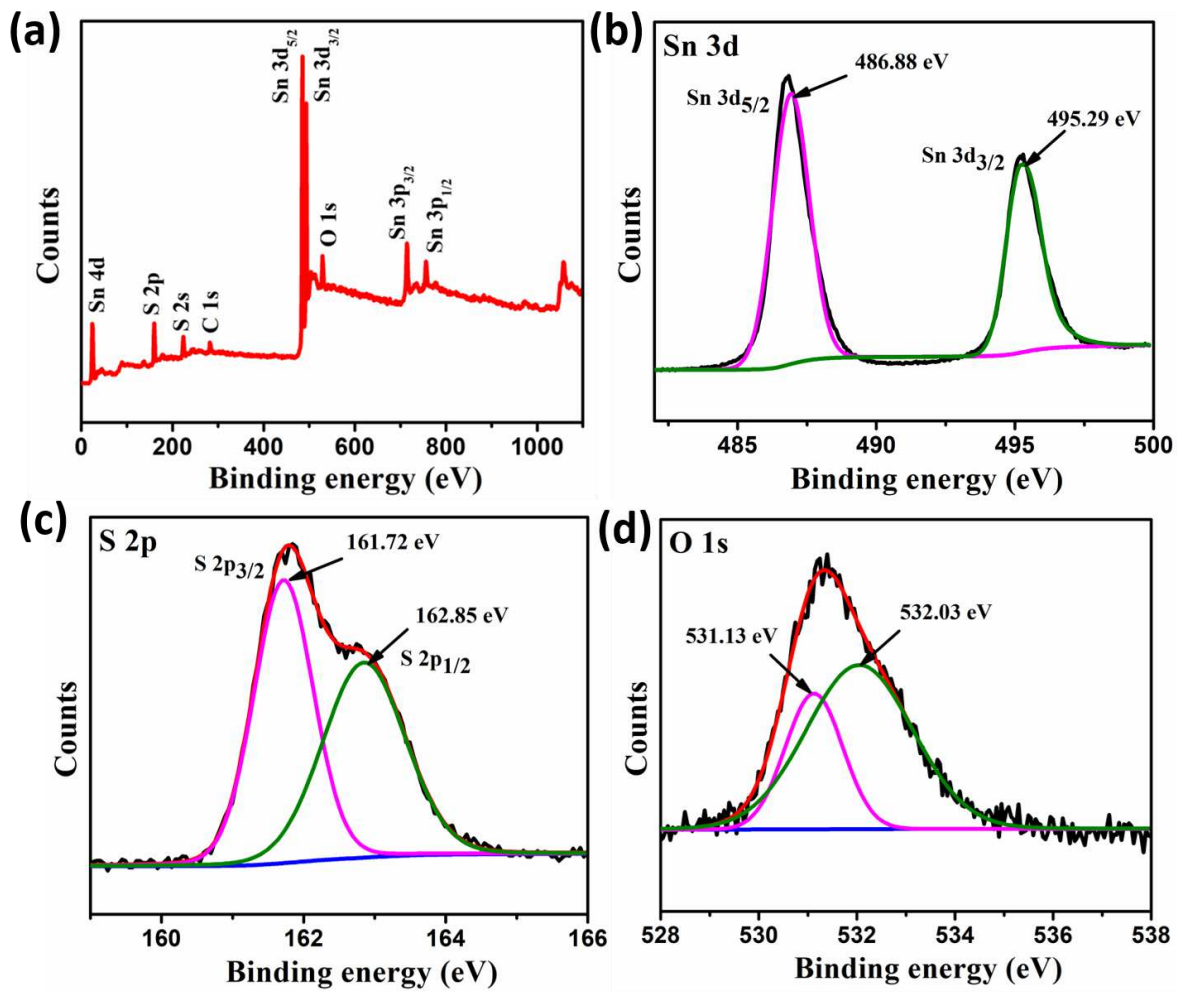


Fig. 3.

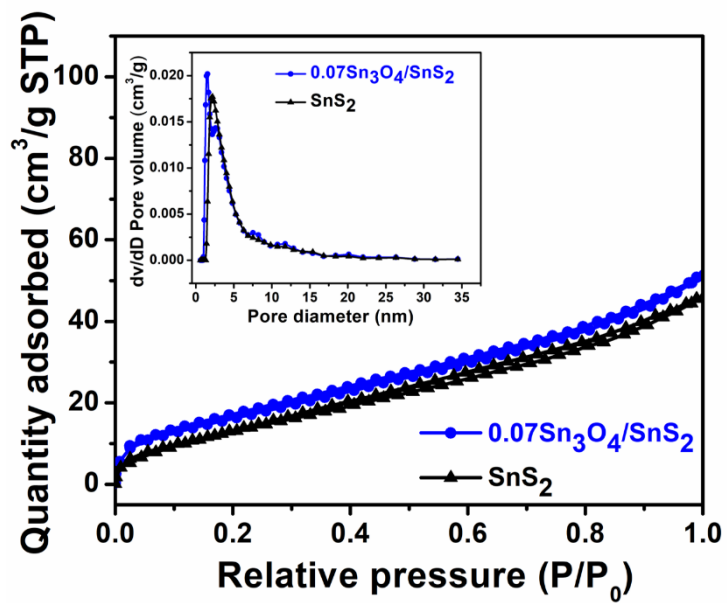


Fig. 4.

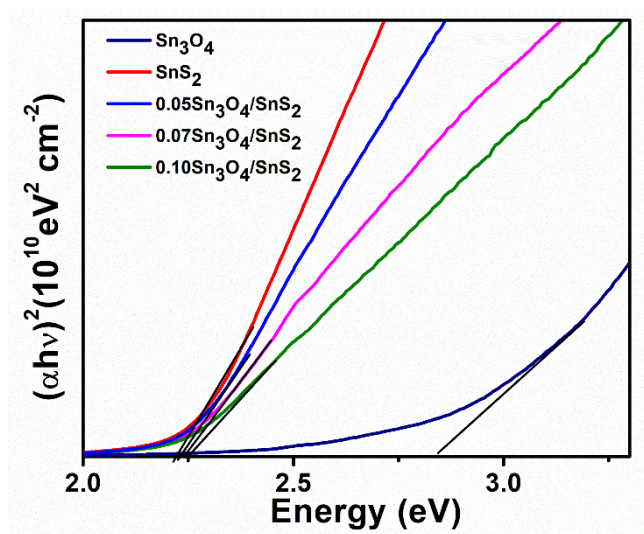


Fig. 5.

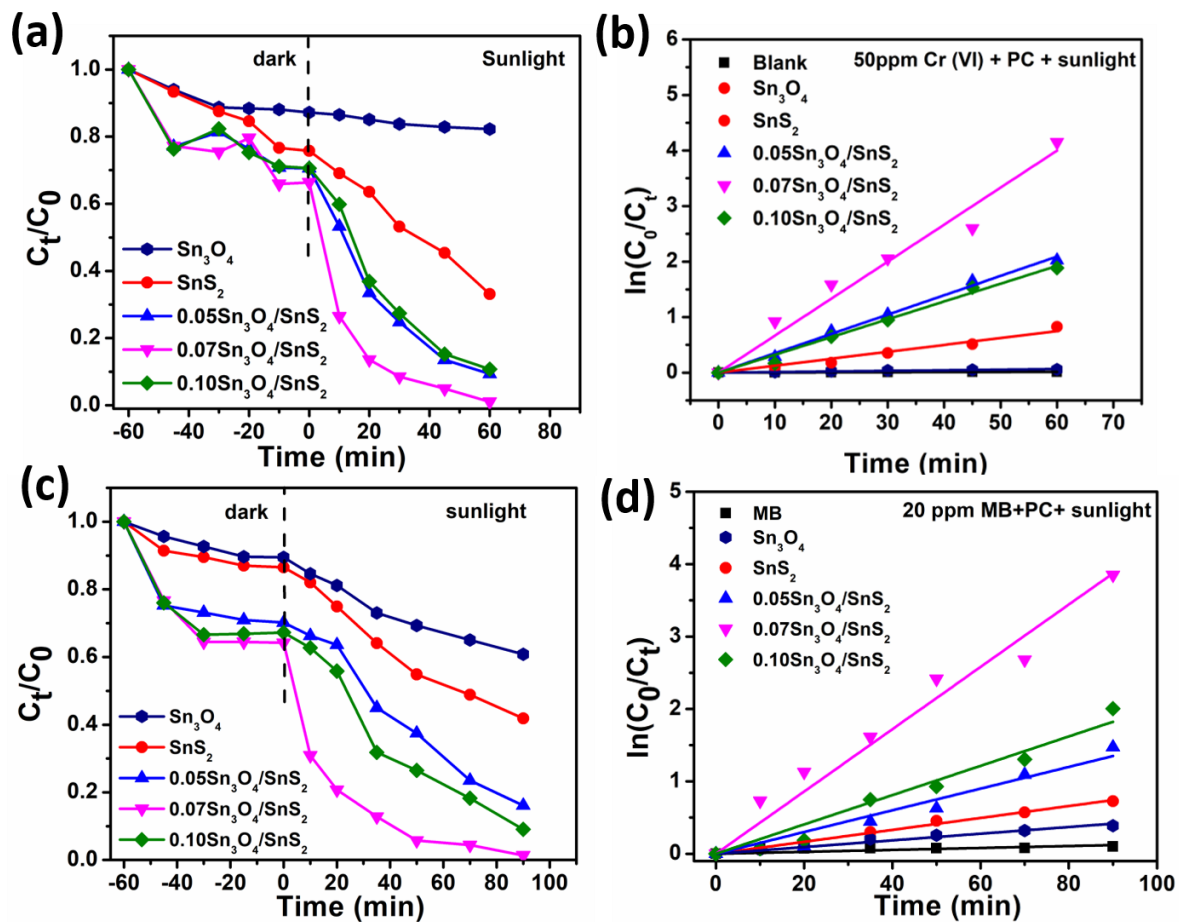


Fig. 6.

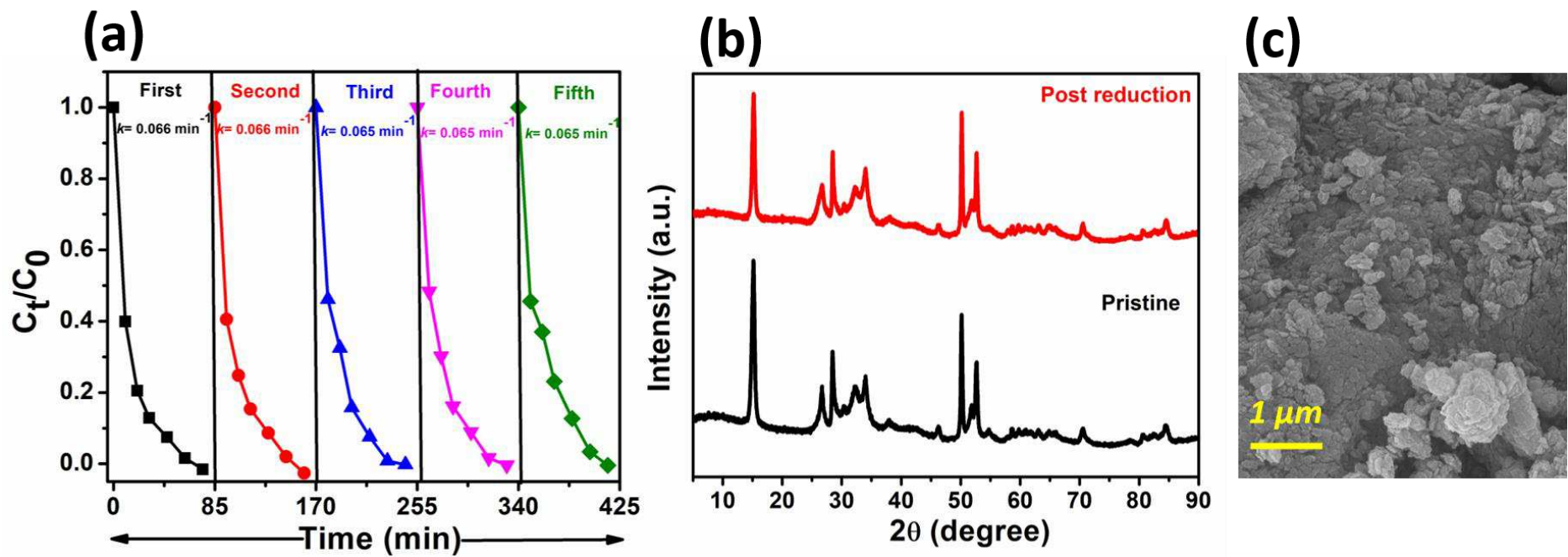


Fig. 7.

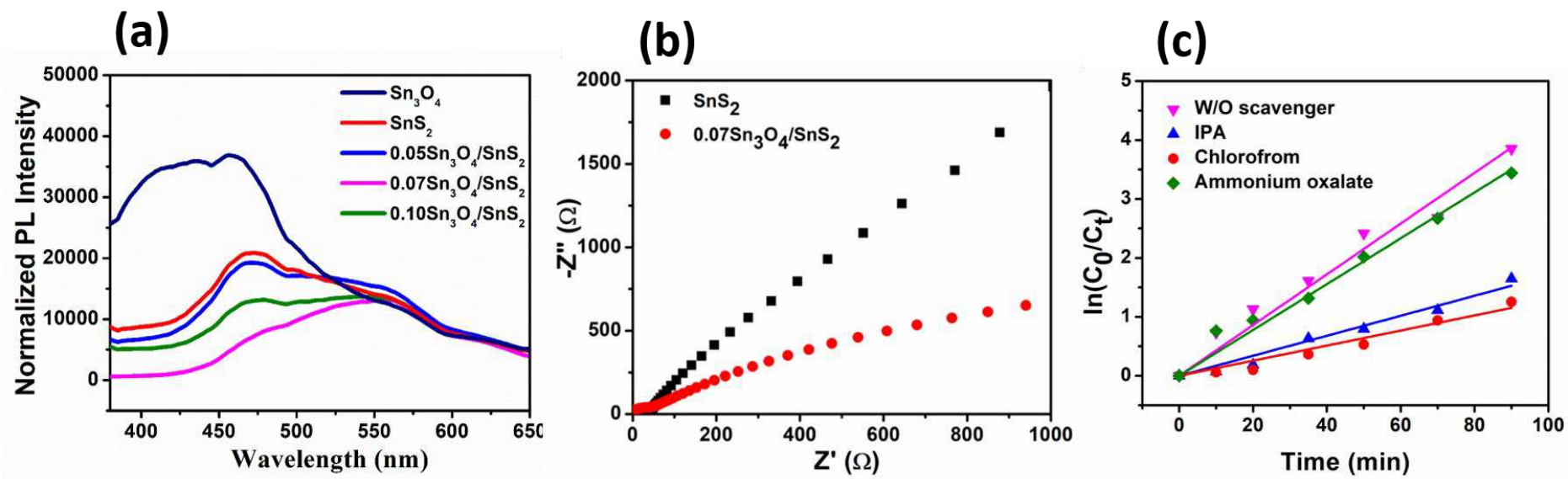
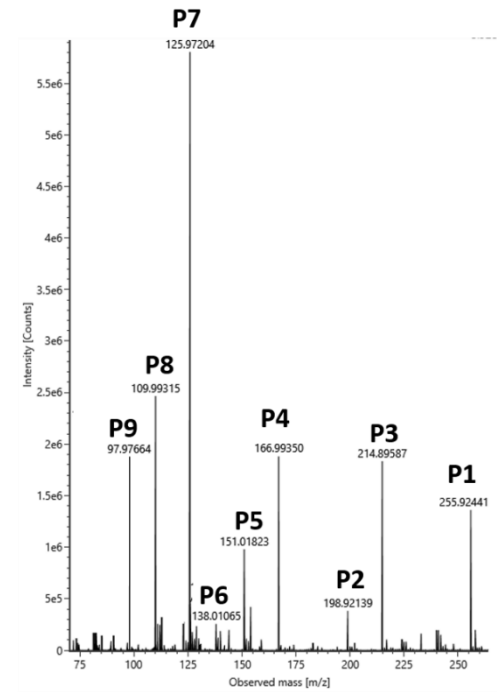
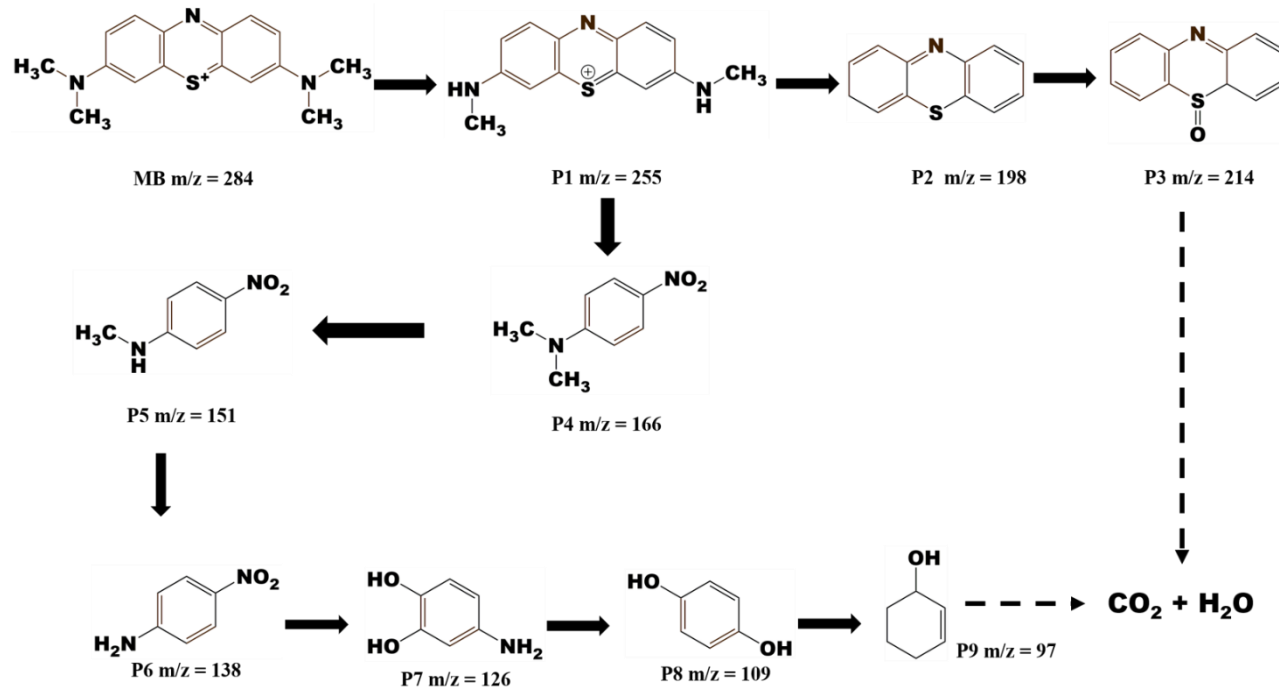
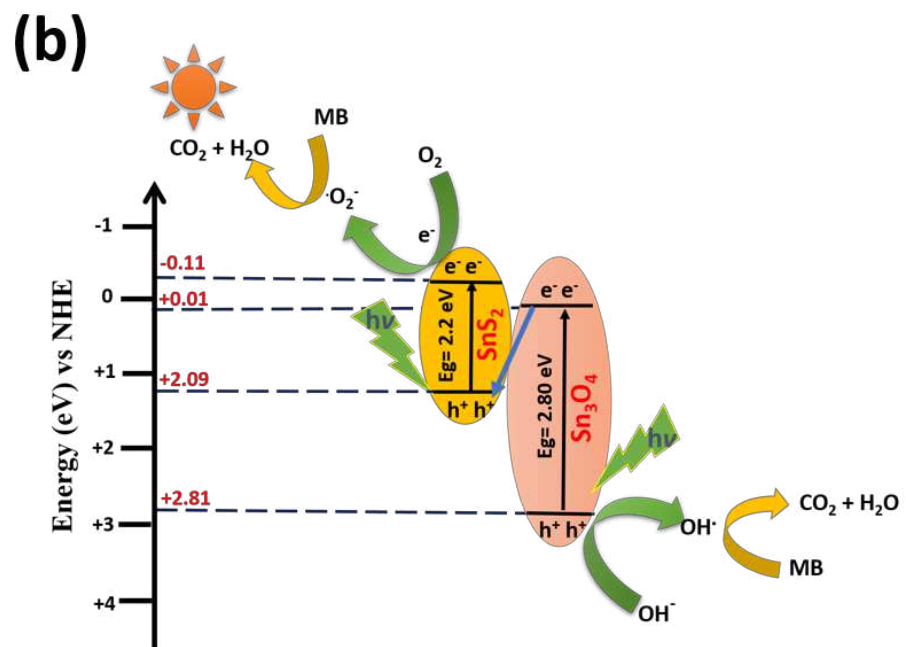
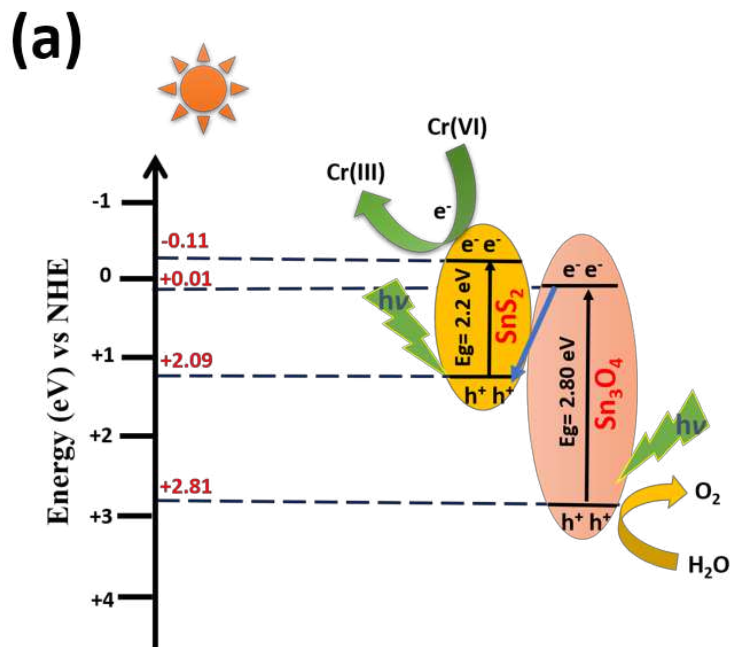


Fig. 8.



Scheme 1.



Scheme 2.

## Supplementary Files

This is a list of supplementary files associated with this preprint. Click to download.

- [SI.docx](#)